

Strong-coupling perturbation theory of the Hubbard model

 S. Pairault¹, D. Sénéchal^{1,a}, and A.-M.S. Tremblay^{1,2}
¹ Centre de Recherche sur les Propriétés Électroniques de Matériaux Avancés et Département de Physique, Université de Sherbrooke, Sherbrooke, Québec, Canada J1K 2R1

² Institut canadien de recherches avancées, Université de Sherbrooke, Sherbrooke, Québec, Canada J1K 2R1

Received 25 October 1999

Abstract. The strong-coupling perturbation theory of the Hubbard model is presented and carried out to order $(t/U)^5$ for the one-particle Green function in arbitrary dimension. The spectral weight $A(\mathbf{k}, \omega)$ is expressed as a Jacobi continued fraction and compared with new Monte-Carlo data of the one-dimensional, half-filled Hubbard model. Different regimes (insulator, conductor and short-range antiferromagnet) are identified in the temperature-hopping integral (T, t) plane. This work completes a first paper on the subject (Phys. Rev. Lett. **80**, 5389 (1998)) by providing details on diagrammatic rules and higher-order results. In addition, the non half-filled case, infinite resummations of diagrams and the double occupancy are discussed. Various tests of the method are also presented.

PACS. 71.10.Fd Lattice fermion models (Hubbard model, etc.) – 71.10.Hf Non-Fermi-liquid ground states, electron phase diagrams and phase transitions in model systems – 71.10.Ca Electron gas, Fermi gas

1 Introduction

The study of strongly-correlated electrons has become in the last decade one of the most active fields of condensed matter physics. The electronic properties of an increasing body of materials cannot be described adequately by Landau's theory of weakly-interacting quasiparticles (Fermi liquid theory) [1,2]. Best known are the high- T_c superconductors and organic conductors. In both cases, a strong anisotropy and a narrow conduction band contribute to make the effects of interactions between electrons (mainly Coulomb repulsion) dramatic.

From a theoretical point of view, quasi-one dimensional (*e.g.* organic conductors) and quasi-two dimensional (*e.g.* high- T_c superconductors) systems are quite different. In one dimension, it is possible to solve satisfactorily a great number of models: lattice Hamiltonians such as the Hubbard model [3] can be solved exactly by Bethe Ansatz [4], whereas nonperturbative results can be obtained for the Tomonaga-Luttinger [5,6] and the g -ology models from bosonization [7] and renormalization-group techniques [8,9]. Conformal field theory has been applied as well, in particular to the Hubbard model [10,11], whose Bethe Ansatz solution has limited practical utility. A unified phenomenology of the so-called Luttinger liquids emerges from these works, whose most striking feature is probably spin-charge separation [12].

On the other hand, the above methods and results cannot be generalized to the case of two dimensions, relevant

to the CuO_2 planes present in all high- T_c superconductors. With a half-filled conduction band, all the parent compounds of the cuprates are antiferromagnetic insulators, and the main challenge is to understand, first towards which kind of metal they evolve upon doping, and secondly whether superconductivity can occur, without a phonon-mediated coupling, in the vicinity of this antiferromagnetic phase. Moreover, the linear temperature dependence of the resistivity [13] is a strong experimental indication that the normal phase of high- T_c superconductors is not a Fermi liquid.

In this context, the Hubbard model [3]

$$\mathcal{H} = -t \sum_{\langle i,j \rangle \sigma} c_{i\sigma}^\dagger c_{j\sigma} + U \sum_i c_{i\uparrow}^\dagger c_{i\downarrow}^\dagger c_{i\downarrow} c_{i\uparrow} \quad (1)$$

has spurred renewed interest for its ability to account for antiferromagnetic correlations and the Mott metal-insulator transition. It is also the simplest model of interacting electrons. In equation (1), t represents the hopping amplitude between two neighboring sites in a tight-binding approximation, and U the strength of the very effectively screened (and thus taken to be local) Coulomb repulsion. At half-filling and for $t \ll U$, the Hubbard model is equivalent to a Heisenberg model with antiferromagnetic exchange $J = 4t^2/U$, and its ground state has long-range Néel order in any dimension $d \geq 2$. A Mott transition can occur towards a metallic state either upon doping, or by increasing the ratio t/U . Thus, the Hubbard model is the prototype of strongly-correlated electrons systems and has been intensely studied, although

^a e-mail: dsenech@physique.usherb.ca

a more realistic model of the CuO_2 planes of the cuprates should involve several bands [14].

Solving the Hubbard model is a difficult problem by itself, even in dimension $d = 1$, where the complexity of the Bethe Ansatz solution prevents one from actually computing most physical quantities. For example, its spectral weight is known only in the limit $U \rightarrow \infty$ and at zero temperature [15]. In any dimension $d \geq 2$, only approximate [3, 16–19] or numerical [20–25] methods are available. Only in the limit $d \rightarrow \infty$ do important simplifications occur [26], allowing to compute most physically interesting quantities in an essentially exact way [27, 28]. In particular, the Mott transition has been studied in great detail, and is still under discussion [29, 30]. Strong coupling perturbation theory, which considers the interaction term of the Hamiltonian as dominant, and the kinetic term as a perturbation, has been somewhat neglected so far. There was some pioneering work of Harris and Lange [31] using the moment technique, but that method cannot easily be pushed to higher order in t . Others have obtained perturbative series for the thermodynamical potential up to order t^4 [32–34], but these approaches do not yield dynamical correlation functions. An original method effectively achieving infinite summations of terms, the so-called Grassmannian Hubbard-Stratonovich transformation, was introduced independently by Bourbonnais [35] and Sarker [36], but contained great difficulties which were overcome only recently [37] by the authors. The purpose of the present paper is to develop the ideas of reference [37] in greater detail, and to present new results that have been obtained in the meantime.

Although we are naturally interested in the two-particle correlation functions (magnetic susceptibility, conductivity, compressibility) and the phase transitions of the Hubbard model, it has proven simpler to first elucidate one-particle properties. Furthermore, spin-charge separation in $d = 1$ is mostly visible in the spectral weight [38, 39], and it is possible to gain significant insight into the metal-insulator transition [14] and antiferromagnetic correlations from the spectral weight alone. Thus, we will focus on the one-particle properties of the Hubbard model throughout most of this paper. From an experimental point of view, angle-resolved photoemission spectroscopy (ARPES) is the probe of choice to measure the spectral weight. Experiments have recently been conducted on quasi one-dimensional SrCuO_2 [40] and NaV_2O_5 [41], and on quasi two-dimensional $\text{SrCuCl}_2\text{O}_2$ [42] antiferromagnetic compounds, and further analyzed with the help of exact diagonalizations [43] and with an application of the methods of the present paper to the $t - t' - U$ model [44].

In Section 2, we present the strong-coupling expansion for dynamical correlation functions, and provide explicit examples of diagram calculation in Appendix A. The method is applied to the half-filled Hubbard model in Section 3, and the resulting spectral weight and double-occupation are compared to Monte-Carlo data in Section 4. Partially self-consistent solutions, involving an infinite sum of diagrams, are investigated in Section 5,

and the question of doping addressed in Section 6. Appendix B provides the atomic one- and two-particle correlation functions, necessary to apply the method, and Appendix C presents a practical test of the method on a toy model. Higher-order terms of the expansion are given in Appendix D.

2 The strong-coupling expansion

In this section we derive the strong-coupling expansion of correlation functions for a wide class of Hamiltonians. We first specify the form that the Hamiltonian should have in order for the method to work. Then we introduce the Grassmannian Hubbard-Stratonovich transformation, and the diagrammatic perturbation theory itself.

2.1 The Hamiltonian

Consider a Hamiltonian $\mathcal{H} = \mathcal{H}^0 + \mathcal{H}^1$, where the unperturbed part \mathcal{H}^0 is diagonal in a certain variable i (for instance a site variable), and let us denote collectively by σ all the other variables of the problem (for instance a spin variable). From now on we will call i the “site variable” and σ the “spin variable” for definiteness, though they may represent any set of quantum numbers. This Hamiltonian describes the behavior of fermions, and we suppose that it is normal-ordered in terms of the annihilation and creation operators $c_{i\sigma}^{(\dagger)}$. \mathcal{H}^0 may be written as a sum over i of on-site Hamiltonians involving only the operators $c_{i\sigma}^{(\dagger)}$ at site i :

$$\mathcal{H}^0 = \sum_i h_i(c_{i\sigma}^\dagger, c_{i\sigma}). \quad (2)$$

Whenever doing actual calculations, we will use the Hubbard model. For the latter, \mathcal{H}^0 corresponds to the atomic limit, that is

$$h_i(c_{i\sigma}^\dagger, c_{i\sigma}) = U c_{i\uparrow}^\dagger c_{i\downarrow}^\dagger c_{i\downarrow} c_{i\uparrow}. \quad (3)$$

We will use the notation $u = U/2$ throughout this paper for convenience. We suppose that the perturbation \mathcal{H}^1 is a one-body operator:

$$\mathcal{H}^1 = \sum_\sigma \sum_{ij} V_{ij} c_{i\sigma}^\dagger c_{j\sigma}, \quad (4)$$

with V a Hermitian matrix. Here, we suppose in addition that the perturbation is diagonal in the spin variable, but this needs not be the case. For the Hubbard model, \mathcal{H}^1 represents the kinetic term, and V is the matrix of hopping amplitudes.

Introducing the imaginary-time dependent Grassmann fields $\gamma_{i\sigma}(\tau)$, $\gamma_{i\sigma}^*(\tau)$, the partition function at some temperature $T = 1/\beta$ may be written using the Feynman

path-integral formalism:

$$Z = \int [d\gamma^* d\gamma] \exp - \int_0^\beta d\tau \left\{ \sum_{i\sigma} \gamma_{i\sigma}^*(\tau) \left(\frac{\partial}{\partial \tau} - \mu \right) \gamma_{i\sigma}(\tau) + \sum_i h_i(\gamma_{i\sigma}^*(\tau), \gamma_{i\sigma}(\tau)) + \sum_{ij\sigma} V_{ij} \gamma_{i\sigma}^*(\tau) \gamma_{j\sigma}(\tau) \right\}. \quad (5)$$

In order to lighten the notation, we will use the first few Latin letters (a, b, \dots) to denote sets such as (i, σ, τ) , and use bra-ket notation. For instance:

$$\int_0^\beta d\tau \sum_{ij\sigma} V_{ij} \gamma_{i\sigma}^*(\tau) \gamma_{j\sigma}(\tau) = \sum_{ab} V_{ab} \gamma_a^* \gamma_b = \langle \gamma | V | \gamma \rangle. \quad (6)$$

2.2 The Grassmannian Hubbard-Stratonovich transformation

At this point, one could use standard perturbation theory and expand the S -matrix in terms of unperturbed correlation functions. Due to the absence of Wick theorem in the case of a nonquadratic unperturbed Hamiltonian, this approach does not lend itself to a satisfactory diagrammatic theory. One cannot define one-particle irreducibility for the diagrams, and one has to be very careful in order to avoid double counting of certain contributions. For example, Pan and Wang [33], and Bartkowiak and Chao [34] had to deal with over five hundred different diagrams in order to obtain the thermodynamic potential of the Hubbard model up to fourth order. These problems were solved by Metzner [45], who organized the perturbation series as a cumulant expansion, and formulated diagrammatic rules with unrestricted sums over momenta. In this subsection we show that Metzner's results can be obtained in a straightforward fashion and even further simplified by means of a simple transformation on the partition function. This transformation was first proposed by Bourbonnais [35] and applied (at zeroth order) to the Hubbard model by Sarker [36]. Boies *et al.* also used it to study the stability of several Luttinger liquids coupled by an interchain hopping [46].

The Grassmannian Hubbard-Stratonovich transformation amounts to expressing the perturbation part of the exponential as the result of a Gaussian integral over auxiliary Grassmann fields $\psi_{i\sigma}(\tau)$, $\psi_{i\sigma}^*(\tau)$ as follows:

$$\int [d\psi^* d\psi] e^{\langle \psi | V^{-1} | \psi \rangle + \langle \psi | \gamma \rangle + \langle \gamma | \psi \rangle} = \det(V^{-1}) e^{-\langle \gamma | V | \gamma \rangle}. \quad (7)$$

In terms of the auxiliary field, the partition function becomes, up to a normalization factor:

$$Z = Z_0 \int [d\psi^* d\psi] e^{\langle \psi | V^{-1} | \psi \rangle} \left\langle e^{\langle \psi | \gamma \rangle + \langle \gamma | \psi \rangle} \right\rangle_0, \quad (8)$$

where $\langle \dots \rangle_0$ means averaging with respect to the unperturbed Hamiltonian. Denoting by $\langle \dots \rangle_{0,c}$ the cumulant

averages, and owing to the block-diagonality of \mathcal{H}^0 , the average in equation (8) can be rewritten as:

$$\exp \sum_{R=1}^{\infty} \frac{1}{(R!)^2} \sum_{i\{\sigma_l, \sigma'_l\}} \int_0^\beta \prod_{l=1}^R d\tau_l d\tau'_l \psi_{i\sigma_1}^*(\tau_1) \times \psi_{i\sigma_R}^*(\tau_R) \psi_{i\sigma'_R}(\tau'_R) \dots \psi_{i\sigma'_1}(\tau'_1) \times \left\langle \gamma_{i\sigma_1}(\tau_1) \dots \gamma_{i\sigma_R}(\tau_R) \gamma_{i\sigma'_R}^*(\tau'_R) \dots \gamma_{i\sigma'_1}^*(\tau'_1) \right\rangle_{0,c}. \quad (9)$$

We will denote by $G_{a_1 \dots a_R, b_1 \dots b_R}^{R(c)} = (-)^R \langle \gamma_{a_1} \dots \gamma_{a_R} \gamma_{b_R}^* \dots \gamma_{b_1}^* \rangle_{0,(c)}$ the various Green functions of the unperturbed Hamiltonian. The partition function now takes the familiar form

$$Z \propto \int [d\psi^* d\psi] \exp \left\{ -S_0[\psi^*, \psi] - \sum_{R=1}^{\infty} S_{\text{int}}^R[\psi^*, \psi] \right\}, \quad (10)$$

where the action has a free (Gaussian) part

$$S_0[\psi^*, \psi] = -\langle \psi | V^{-1} | \psi \rangle, \quad (11)$$

and an infinite number of interaction terms [47]

$$S_{\text{int}}^R[\psi^*, \psi] = \frac{-1}{(R!)^2} \sum'_{\{a_l, b_l\}} \psi_{a_1} \dots \psi_{a_R} \psi_{b_R}^* \dots \psi_{b_1}^* G_{a_1 \dots a_R, b_1 \dots b_R}^{Rc}. \quad (12)$$

The primed summation in equation (12) reminds us that all the fields in a given term of the sum share the same value of the site index. The free propagator for the auxiliary fermions is just V , and we may now use Wick's theorem to derive diagrammatic rules in order to treat the interaction terms perturbatively. Appendix A gives a thorough description of the diagrammatic rules as well as two explicit examples of application to the one-particle Green function and the thermodynamical potential.

One may wonder why we did not include the first interaction term into the free part of the action $S_0[\psi^*, \psi]$, since it is quadratic in the field ψ . The reason is that we want to count precisely the order of a given diagram in the perturbation V . By separating the free and interacting parts of the action as in equations (11, 12), the order of a given diagram is simply the number of ψ propagators, whereas the alternate method mixes all powers of V from zero to infinity. This question will be discussed more thoroughly in Section 5 below.

2.3 Electron Green functions

We now show how to deduce the correlation functions of the original electrons (γ) from those of the auxiliary fermions (ψ) to which the perturbation theory applies. When coupling the electron field γ to an external

Grassmannian source J_a^* , J_a , the partition function takes the form (very similar to Eq. (8)):

$$Z(J^*, J) = \int [d\psi^* d\psi] e^{\langle \psi | V^{-1} | \psi \rangle} \left\langle e^{\langle \psi + J | \gamma \rangle + \langle \gamma | \psi + J \rangle} \right\rangle_0. \quad (13)$$

A $2R$ -point correlation function reads

$$\begin{aligned} \mathcal{G}_{b_1 \dots b_R}^{R a_1 \dots a_R} &= (-)^R \langle \gamma_{a_1} \dots \gamma_{a_R} \gamma_{b_R}^* \dots \gamma_{b_1}^* \rangle \\ &= \frac{1}{Z} \int [d\psi^* d\psi] \left[\frac{\delta \langle e^{\langle \psi + J | \gamma \rangle + \langle \gamma | \psi + J \rangle} \rangle_0}{\delta J_{a_1}^* \dots \delta J_{a_R}^* \delta J_{b_R} \dots \delta J_{b_1}} \right]_{J^*=0, J=0} \\ &\quad \times e^{\langle \psi | V^{-1} | \psi \rangle}. \end{aligned} \quad (14)$$

Noticing that

$$\left[\frac{\delta \langle e^{\langle \psi + J | \gamma \rangle + \langle \gamma | \psi + J \rangle} \rangle_0}{\delta J_{a_1}^* \dots \delta J_{a_R}^* \delta J_{b_R} \dots \delta J_{b_1}} \right]_{J^*=0, J=0} = \frac{\delta \langle e^{\langle \psi | \gamma \rangle + \langle \gamma | \psi \rangle} \rangle_0}{\delta \psi_{a_1}^* \dots \delta \psi_{a_R}^* \delta \psi_{b_R} \dots \delta \psi_{b_1}}, \quad (15)$$

we perform $2R$ integrations by parts, and obtain:

$$\begin{aligned} \mathcal{G}_{b_1 \dots b_R}^{R a_1 \dots a_R} &= \frac{(-)^R}{Z} \int [d\psi^* d\psi] \left(\frac{\delta e^{\langle \psi | V^{-1} | \psi \rangle}}{\delta \psi_{b_1} \dots \delta \psi_{b_R} \delta \psi_{a_R}^* \dots \delta \psi_{a_1}^*} \right) \\ &\quad \times \left\langle e^{\langle \psi | \gamma \rangle + \langle \gamma | \psi \rangle} \right\rangle_0, \end{aligned} \quad (16)$$

which expresses \mathcal{G}^R in terms of correlation functions of the ψ field. For instance, a straightforward calculation gives the relation between the Green functions $\mathcal{G}_{ab} = -\langle \gamma_a \gamma_b^* \rangle$ and $\mathcal{V}_{ab} = -\langle \psi_a \psi_b^* \rangle$, which we write in matrix form

$$\mathcal{G} = -V^{-1} + V^{-1} \mathcal{V} V^{-1}. \quad (17)$$

If Γ denotes the self-energy of the auxiliary field, then

$$\mathcal{G} = (\Gamma^{-1} - V)^{-1}. \quad (18)$$

Likewise, a connected 2-point correlation function of the original fermions is the corresponding amputated, connected 2-point correlation function of the auxiliary fermions.

$$\begin{aligned} \mathcal{G}_{a_1 a_2, b_1 b_2}^{\text{IIC}} &= (V^{-1})_{a_1 a_1'} (V^{-1})_{a_2 a_2'} \mathcal{V}_{a_1' a_2', b_1' b_2'}^{\text{IIC}} \\ &\quad \times (V^{-1})_{b_1' b_1} (V^{-1})_{b_2' b_2}, \end{aligned} \quad (19)$$

where a summation over repeated indices is implicit on the right-hand side.

To conclude this section, let us summarize our line of thought up to now. We wish to compute physical quantities within a strongly correlated fermion model (say, the Hubbard model). Given that the energy of the interaction is greater than the bandwidth, we want to build a strong-coupling expansion. Ordinary perturbation theory turns out to be quite cumbersome, but the simple transformation (7) restores Wick's theorem and a (nearly standard) diagrammatic approach for the auxiliary fermions. Finally, the simple relations (17–19) make the connection back to electron Green functions.

3 Application to the half-filled Hubbard model

We apply the method presented in the previous section to the Hubbard model at half filling in any dimension. When doing so, we first have to deal with an unexpected causality problem, whose solution can be viewed as part of the method itself. Then we compute the spectral function and the density of states, and discuss their relevance to the Mott metal-insulator transition and to antiferromagnetic correlations.

3.1 Lehmann representability and the one-particle Green function up to order three

The simplest dynamical quantity amenable to our method is the one-particle spectral function:

$$A(\mathbf{k}, \omega) = \lim_{\eta \rightarrow 0^+} -2 \text{Im} \mathcal{G}(\mathbf{k}, \omega + i\eta). \quad (20)$$

It is the simplest energy and wavevector resolved correlation function. As such, it contains a lot of physical information, far more detailed than the density of states, which is only its momentum-integrated version. It is also the best tool to investigate the Fermi liquid character of the system, *i.e.*, whether or not it is dominated by a narrow peak at the Fermi level. Finally, it is very badly known from a theoretical (and numerical) point of view, whereas experiments of angle-resolved photoemission have recently become more reliable and precise. To obtain the Green function, we have to compute the self-energy Γ of the auxiliary fermions. From now on we will use the nearest-neighbor Hubbard model

$$\begin{aligned} \mathcal{H} &= -t \sum_{\langle i,j \rangle \sigma} c_{i\sigma}^\dagger c_{j\sigma} + 2u \sum_i c_{i\uparrow}^\dagger c_{i\downarrow}^\dagger c_{i\downarrow} c_{i\uparrow} \\ &\quad \left(u \equiv \frac{U}{2} \right), \end{aligned} \quad (21)$$

which means that $V(\mathbf{k}) = -2tc(\mathbf{k})$, where $c(\mathbf{k}) = \sum_{m=1}^d \cos k_m$. Throughout this section, we work at half-filling by setting the chemical potential to $\mu = u = U/2$. The simplest diagram contributing to Γ , of order zero in t , is just the atomic Green function

$$\Gamma^{(0)}(\mathbf{k}, i\omega) = G(i\omega) = \frac{i\omega}{(i\omega)^2 - u^2}, \quad (22)$$

where $i\omega$ stand for a complex frequency (we keep the symbol ω for a real frequency). This leads to the following approximate Green function:

$$\mathcal{G}^{(1)}(i\omega) = \frac{1}{\frac{(i\omega)^2 - u^2}{i\omega} + 2tc(\mathbf{k})}. \quad (23)$$

One recognizes in equation (23) the result of the Hubbard-I approximation [3], whose properties are well-known. The original atomic levels at $\pm u$ are spread out by the hopping

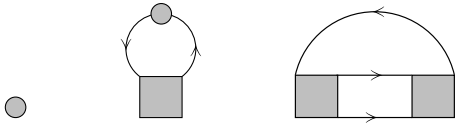


Fig. 1. Diagrams contributing to the self-energy Γ of the auxiliary fermions up to order t^3 .

term into two symmetric bands called Hubbard bands. The lower band has band edges at $\pm 2td - \sqrt{(2td)^2 + u^2}$ and never reaches the Fermi level, however large t may be. Thus, this approximation fails to describe the Mott metal-insulator transition. But in the method used here, the Hubbard-I approximation simply stems from the zeroth order value of Γ , and we know a systematic way of improving it.

The diagrams contributing to Γ up to order t^3 are presented in Figure 1. Actually, there are more diagrams at this order, but they vanish due to the precise form of $V(\mathbf{k})$. To compute these diagrams, we need the explicit expression of $G_{\sigma_1\sigma_2,\sigma_3\sigma_4}^{\text{IIc}}(i\omega_1, i\omega_2; i\omega_3, i\omega_4)$. The calculation of this atomic correlation function is a bit cumbersome, though simple in principle. The main result as well as several useful remarks are presented in Appendix B. For the time being, let us focus on the result:

$$\Gamma^{(3)}(\mathbf{k}, i\omega) = \frac{i\omega}{(i\omega)^2 - u^2} + \frac{6t^2 du^2 i\omega}{((i\omega)^2 - u^2)^3} + 6t^3 c(\mathbf{k}) \left(\frac{\frac{\beta u}{2} \tanh\left(\frac{\beta u}{2}\right)}{((i\omega)^2 - u^2)^2} + \frac{u^2 (2(i\omega)^2 - u^2)}{((i\omega)^2 - u^2)^4} \right). \quad (24)$$

By injecting the above approximate value of Γ into equation (18) for the Green function, one obtains a rational function of $i\omega$, presenting a finite number of poles in the complex plane. Such a result is already somewhat disappointing since it cannot account for a continuous spectral weight. But more seriously, the Green function presents pairs of complex conjugate poles away from the real axis, and as a consequence does not verify Kramers-Krönig relations. Furthermore, for a wavevector verifying $V(\mathbf{k}) = 0$, the Green function is equal to Γ itself, and has high-order poles at $\pm u$, leading to negative spectral weight. So by simply replacing Γ by its approximate value to third order in t in equation (18), one ends up with a noncausal Green function, whose spectral function is neither positive, nor normalized.

Any Green function acceptable on physical grounds should be causal and have a positive spectral weight, *i.e.*, be a sum (finite or infinite) of simple real poles with positive residues. We call such a function Lehmann representable since these properties are proven rigorously using the Lehmann representation of the exact Green function. The way out of the problems mentioned in the previous paragraph is to recall that the power series expansion of the Lehmann representation of the exact Green function should give, order by order, the same expansion of \mathcal{G} as that obtained by diagrams, and this for all values of frequency. This simple observation will allow us to build back

a Lehmann representable function from the power series, as shown below.

The systematic way of building a Lehmann representable function whose power series equals that of \mathcal{G} is provided by a theorem reported in reference [48]: a rational function is Lehmann representable if and only if it can be written as a Jacobi continued fraction

$$\mathcal{G}_J(i\omega) = \frac{a_0}{i\omega + b_1 -} \frac{a_1}{i\omega + b_2 -} \cdots \frac{a_{n-1}}{i\omega + b_n}, \quad (25)$$

with

$$b_l \text{ real and } a_l > 0. \quad (26)$$

In any finite system, the exact Green function can be cast into the form (25) with a finite value of n (the number of floors of the continued fraction). If we consider the coefficients a_l and b_l as functions of t and expand $\mathcal{G}_J(i\omega)$ in powers of t , we should obtain the same power series as that of \mathcal{G} but at the price of destroying the continued fraction structure, and creating, in general, an approximation that suffers from causality and normalization problems. On the other hand, if the power series in t for the coefficients themselves are left where they belong in $\mathcal{G}_J(i\omega)$, we can still expect their truncated Taylor series to verify conditions equation (26), and consequently the perturbative $\mathcal{G}_J(i\omega)$ obtained this way to be Lehmann representable.

The objective, then, is to obtain in a unique way the power series for a_l and b_l from that of \mathcal{G} and use the corresponding $\mathcal{G}_J(i\omega)$ as our perturbatively calculated Green function. For practical calculations, it is useful to know that there exists a double recurrence relation giving the a_l and b_l starting from the moments of the function. Since we know the exact Taylor expansion of \mathcal{G} up to order t^3 , we know all its spectral moments to the same order. So we simply need to work out the recurrence relations and compute the coefficients of the continued fraction up to the order available. Once an a_l is found to be zero to the best of our knowledge – that is, if it contributes to the full \mathcal{G}_J , given the preceding coefficients, at an order higher than the working precision (t^3 in this section) – we may truncate the continued fraction. In all the cases that we treated, such an a_l always occurred rather quickly (the deepest continued fraction we had to deal with had eight floors). This means that the density of poles is always weak, and the poles remain essentially well separated: they cannot account for the precise shape of a continuous spectral weight, but can sample it adequately (the moments of the distribution are well represented). More important, the Green function $\mathcal{G}_J(i\omega)$ thus obtained is unique at any given order in perturbation theory and is causal as long as conditions (26) are satisfied by the perturbative expression for a_l and b_l .

In order to test both the diagrammatic theory and the continued fraction representation, we treated the exactly solvable case of the atomic limit itself, away from half-filling. Indeed, setting the chemical potential to $\mu = u + t_0$, one can either compute the exact Green function, then expand the solution in powers of t_0 , or notice that the shift

of chemical potential has the form of a zero-range hopping and obtain the t_0 expansion from diagrams. This procedure is presented in Appendix C, and leads to the following main conclusions: the diagrams actually give the correct answer, which however presents the same causality problems as already mentioned, and the continued fraction representation properly builds back the poles and the residues of the exact solution. We also tested our approach on the (again exactly solvable) two-site problem, where the same conclusions apply.

The above considerations also shed new light on the usual weak-coupling perturbation theory. In that case too, one gets multiple poles when truncating the series for \mathcal{G} , and the way out of this difficulty is to use Dyson's equation – valid because Wick's theorem applies directly to the original fermions – and to compute the self-energy. If the self-energy is Lehmann representable, that is, if it possesses an underlying continued fraction structure, then the Green function will inherit this structure from it and will be Lehmann representable too. We did not find any definite answer as to why the self-energy itself, as obtained from a few diagrams, turns out to be acceptable in general, but there are some plausible explanations. One is that the unperturbed case already presents a continuum of levels, instead of only two. So if a double pole appears in the expression of a diagram, it is likely that its isolated contribution will be negligible in the thermodynamic limit. Also, the vertices of weak-coupling theories are often local in time or, if retarded, depend only on two times, whereas here the vertices have a full dependence on all frequencies entering them, which is quite peculiar. Finally, nothing proves that a finite-order weak-coupling self-energy is always Lehmann representable, and counter-examples may well exist.

Applying the above procedure to the result (24) yields the following continued fraction:

$$\mathcal{G}_J(\mathbf{k}, i\omega) = \frac{1}{i\omega + 2tc(\mathbf{k}) - \frac{u^2}{i\omega - 3\beta t^3 \tanh(\beta u/2)c(\mathbf{k})/u - \frac{6t^2 d}{i\omega - 2tc(\mathbf{k})/d - \frac{u^2}{i\omega + tc(\mathbf{k})/d}}}, \quad (27)$$

which has exactly the same Taylor expansion as the exact Green function up to order t^3 , verifies the conditions (26), and is normalized to unity. The next two subsections show that the spectral weight deduced from equation (24) describes the Mott metal-insulator transition, and the appearance of strong antiferromagnetic correlations at low temperature in the Hubbard model.

3.2 The Mott transition

Strictly speaking, there is no agreed upon definition of the Mott transition in terms of one-particle properties only. But one can use as a heuristic criterion (even at nonzero temperature) the appearance of spectral weight at the Fermi level. With the normalization (20) of the spectral

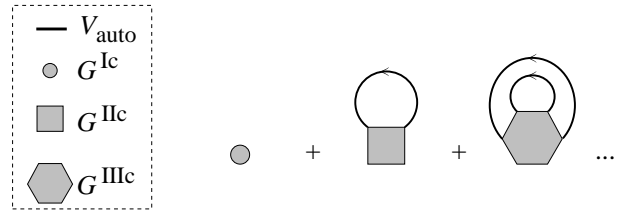


Fig. 2. Diagrams yielding the exact $\Gamma(i\omega)$ when $d \rightarrow \infty$. $V_{\text{auto}}(\mathbf{k}, i\omega) = V(\mathbf{k})/(1 - \Gamma(i\omega)V(\mathbf{k}))$ is itself dressed with these diagrams.

weight, the density of states has the following expression:

$$N(\omega) = \int_{-\pi}^{\pi} \frac{d^d k}{(2\pi)^d} A(\mathbf{k}, \omega). \quad (28)$$

We observe that in the density of states, as t increases from zero, the two symmetric Hubbard bands – reduced to two delta functions at $\pm u$ in the atomic limit – widen, and eventually mix for t beyond some critical value. At high temperature ($T > u$), the gap is closed by excitations of momentum $\mathbf{k} = (0, \dots, 0)$ and $\mathbf{k} = (\pi, \dots, \pi)$, making it possible to compute the exact value of the critical hopping:

$$t_c = u \frac{\sqrt{1 + \sqrt{1 + 12d^2}}}{2d\sqrt{3}}. \quad (29)$$

This gives $U_c \simeq 3.2t$ for $d = 1$, to be compared with $U_c \simeq 3.5t$ found in the Hubbard-III approximation. Note that t_c scales properly with the dimension, and leads to $U_c = 1.86t^*$ (with $t^* = 2t\sqrt{d}$) in the limit of infinite dimension. This critical value of interaction strength is too large [27, 49] for two reasons. First, when $d \rightarrow \infty$ our criterion corresponds to subbands that meet with an exponentially small density of states, therefore not yet truly closing the gap. Secondly, when $d \rightarrow \infty$, the order of a diagram has to be counted in a different way. Any nonlocal contribution becomes negligible, as is visible for example on the contributions of the third-order term of equation (24) to the continued fraction equation (27). Actually, the exact solution in $d \rightarrow \infty$ is given by the diagrams depicted in Figure 2, as was mentioned in reference [45]. Therefore, the approximation (24) becomes quite crude in infinite dimension. Note that our criterion for the Mott transition differs from that used in $d \rightarrow \infty$, since we simply demand the closure of the gap at the Fermi level, without requiring the appearance of a new coherent peak in $A(\mathbf{k}, \omega)$ at $\omega = 0$. Such a peak does not appear in the present approach.

When $T < u$, we cannot calculate t_c analytically because we do not know which excitations close the gap, but Figure 3 sketches a numerical evaluation (for $d = 1$) in the (T, t) plane of the line where the gap vanishes. The value of t_c grows upon lowering T , and there is no Mott transition at zero temperature, in agreement with the exact result [4].

One has to keep in mind two important things about the insulator to metal transition described in this subsection. First, if we call \mathbf{Q} the difference between the momentum of the highest negative energy (hole-like) excitation

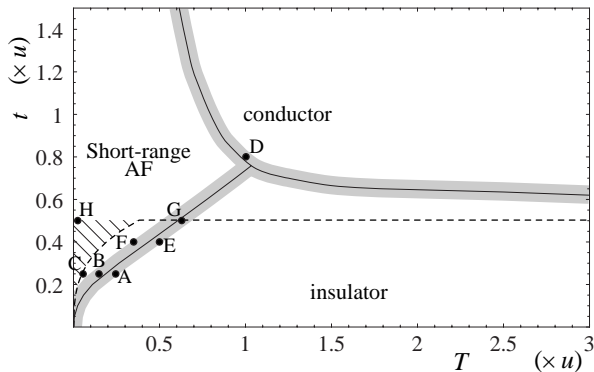


Fig. 3. Crossover diagram of the one-dimensional half-filled Hubbard model as obtained from the third-order Green function. The estimated domain of validity of the approximation is the region under the dot-dashed line.

and that of the lowest positive energy (particle-like) excitation, then \mathbf{Q} takes the value (π, \dots, π) at high temperature, and goes to zero when $T \rightarrow 0$, but the gap always remains indirect. Secondly, even when the gap has been closed, the spectral weight at the Fermi energy still has several well separated peaks. $A(\mathbf{k}, \omega)$ is never dominated at small ω by a single narrow quasiparticle peak allowing to define a Fermi wavevector and a Fermi velocity. Thus, when extrapolating it beyond the transition, our solution does not describe a Fermi liquid. This is not surprising since we do not expect a perturbative method starting from the completely localized insulating state to be able to describe both phases satisfactorily.

3.3 Antiferromagnetic correlations

Here again, a rigorous discussion of the magnetic behavior of the system should be based on the magnetic susceptibility, which is a two-particle function. Nonetheless, the spectral weight should contain a valuable qualitative signature of increased antiferromagnetic correlations, namely a change in its periodicity. Indeed, if there were a true antiferromagnetic ordering of the spins, the doubling of the unit cell should lead to a periodicity of π in reciprocal space, instead of 2π , in all the correlation functions. We expect signs of this reduced periodicity to appear, even in the disordered phase, when antiferromagnetic correlations become strong. Their effect actually show up at low T , as illustrated by the plot of $A(k, \omega)$ of Figure 4, corresponding to point C of Figure 3. For simplicity, we discuss the 1D case in this subsection (\mathbf{k} becomes k), but the conclusions apply to any dimension. We stress that we only observe the appearance of increased correlations but always remain in the disordered state: a true transition towards a long-range ordered state in $d \geq 3$ is not visible in our results, and Figure 3 is by no means a phase diagram, but only a crossover diagram where we distinguished regions of different qualitative behavior of the one-particle spectral function. $A(k, \omega)$ has four delta peaks (a finite width η is added for clarity) given by dispersion relations $\omega_i(k)$, ($i = 1$ to 4, as shown in Fig. 4).

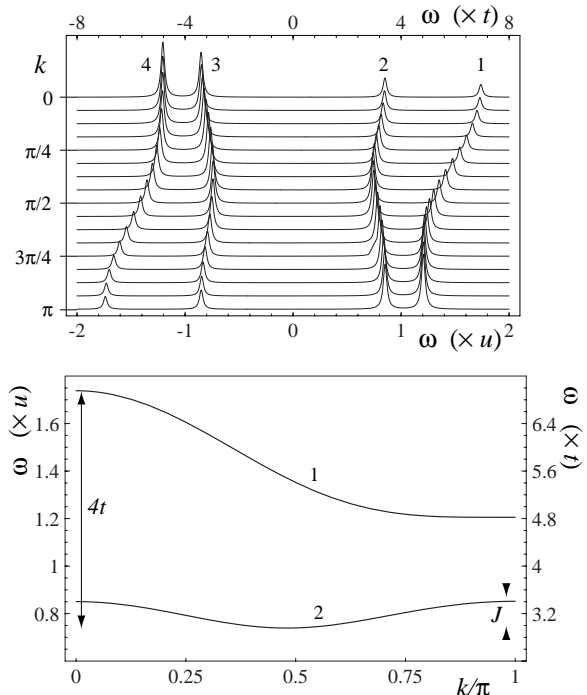


Fig. 4. Spectral weight of the half-filled one-dimensional Hubbard model in the antiferromagnetically correlated regime (point C, $t = 0.25u$, $T = 0.06u = 0.24t$).

The spectral weight is an even function of k , and particle-hole symmetry at half-filling ensures that $A(k + \pi, -\omega) = A(k, \omega)$. The minimum of $\omega_2(k)$ is at $k = 0$ at small t and high T (e.g. point A of Fig. 3). But when T is lowered down to point C (Fig. 4), this minimum moves continuously from $k = 0$ towards $k = \pi/2$, and peak 2 loses weight for values of k much smaller than $\pi/2$. These changes reflect the AF short-range order that gradually builds up when T becomes smaller than the AF superexchange $J = 2t^2/u$ of the equivalent $t - J$ model. As suggested above, the approximate cell doubling in direct space translates into a nearly π -periodic dispersion for peak 2, although the 2π -periodicity of its weight and of $\omega_1(k)$ reminds us that the state remains paramagnetic. We chose to define an AF crossover line in Figure 3 as the points where $k = 0$ ceases to be the minimum of the dispersion $\omega_2(k)$. This crossover line is roughly parabolic ($T \sim t^2$) at low t , which implies a crossover temperature proportional to $J = 2t^2/u$. Furthermore, in this regime, the width of band 2 is of order J whatever the value of t , supporting the above interpretation.

4 Comparison with numerical results and limitations of the method

The purpose of this section is to try and find out where in parameter space – the (T, t) plane – the approximate Green function (27) can be regarded as reliable, to improve it and compare it with Monte-Carlo results when possible. The entire section applies to the half-filled Hubbard model.

4.1 Reliability of the third-order solution

It is not an easy task to define a domain of validity for the present approximation scheme for several reasons. First, the expansion parameter being the hopping amplitude t , any hopping process is considered on an equal footing regardless of whether it involves a change in the double occupancy or not. As a consequence, we expect the ratio t/T to play as important a role as t/u . Secondly the end result involves t in a complicated way, and not only through a power series. Nevertheless, since the atomic Green function is just

$$\frac{1}{i\omega - \frac{u^2}{i\omega}} \quad (30)$$

and gives spectral weight only at $i\omega = \pm u$, we expect an approximation of the form (25) to be valid when the b_l 's of equation (25) are small with respect to u . When applied to equation (27), this criterion leads to the conditions:

$$2dt < u \quad \text{and} \quad \left(\frac{t}{u}\right)^3 < \frac{1}{3d} \left(\frac{T}{u}\right). \quad (31)$$

The first requirement is quite intuitive: it expresses that the bandwidth is smaller than the on-site interaction, which was the basic assumption anyway. The second one gives the low-temperature limitation of the method. In dimension $d = 1$, the region where the two conditions equation (31) are fulfilled lies under the dashed line of Figure 3. When extrapolating the results outside this region, one cannot predict how fast the approximation may deteriorate. In particular, it is worth mentioning that the $t \rightarrow \infty$ (free-particle) limit is recovered properly. On the other hand, at small t the $T \rightarrow 0$ limit again gives a free-particle behavior (except for a singular behavior for wavevectors such that $V(\mathbf{k}) = 0$), which is obviously wrong. This allows us to define, besides the region of (almost) certain validity under the dashed line in Figure 3, a hatched region of acknowledged failure. For the one-dimensional case, the theoretical [39] and exact [15] results describing spin-charge separation fall in this region of parameter space, which prevents us from making any meaningful comparison. However, a definite prediction of our work is that upon raising the temperature, there appears noticeable spectral weight near $k = \pi$ (for $\omega < 0$). This new feature of the spectral weight, visible as peak 3 of Figure 4 and absent from the zero-temperature solutions, might correspond to the ‘‘question-mark’’ features in Figure 1 of reference [40]. Thus, temperature seems to have a drastic effect on the distribution of spectral weight.

4.2 Beyond third order

We have also computed the Green function to fourth and fifth order. Let us stress straight away that one is never certain to improve a perturbative result by adding higher-order terms. Actually, in most of the cases where perturbation theory is used, the series is asymptotic rather than

convergent, and there is an optimal order – typically of the order of the inverse of the expansion parameter – beyond which the approximation deteriorates quickly with each new term [50]. Computing the fourth and fifth order presented a substantial technical difficulty, since it involved the atomic function G^{IIIc} having a different expression for each of the $5! = 120$ possible time orderings (one of the times can be set to zero). We overcame this difficulty by designing a symbolic manipulation program dedicated to this problem, taking advantage of the very systematic form of the expressions in the atomic limit. Let us mention that up to fifth order – and that seems to be general – the even orders lead to a modification of the partial numerators (a_l) only, and the odd orders lead to a modification of the partial denominators (b_l) only, within the continued fraction (25). Appendix D presents the diagrams and the result for $\Gamma(\mathbf{k}, i\omega)$ up to fourth order. $\Gamma(\mathbf{k}, i\omega)$ and the corresponding continued fraction have been computed up to fifth order included, but the analytic expression is too lengthy to be presented: It is available on the internet (Ref. [51]). Plots of the solution will be presented in following sections.

At both orders the Green function has eight poles, among which only six have a significant residue. Thus, there appears only one more pole in each Hubbard band with respect to order t^3 . Furthermore, except for the region where the series certainly converges, the fifth order may give an answer quite different from that of the third or fourth order. In particular, the presence of diverging coefficients makes the self-energy (in the usual sense) go to zero very fast upon lowering the temperature, and the solution then coincides with the free-particle limit, completely missing the antiferromagnetic correlation effect described in Section 3.3. On the other hand, our prediction for the Mott transition is more reliable at fifth order than third order. For instance, Point G of Figure 3 is predicted to be in the insulating phase at third-order, and in the conducting phase at fifth-order. Monte-Carlo simulations at that point show that the latter conclusion is the correct one (Fig. 5).

In order to test the analytic validity of our results, we computed the exact Green function up to fifth order for the exactly solvable two-site problem, and compared with the diagrammatic approach. The two approaches give identical results at fifth order. The test is summarized in Appendix D. In that case, the continued fraction has only four poles instead of eight, as it should. It is interesting to see that in that case too, the best approximation can be the third, fourth, or fifth order, depending on the parameters. Most importantly, the two-site problem confirms that dealing with a small value of t/u is not sufficient to ensure the accuracy of the approximation. As a matter of fact, we observed empirically that higher orders improve the solution for $T > t$, and deteriorate it for $T \ll t$. Explaining precisely why perturbation theory fails at low temperature appears difficult; this is probably related to the huge degeneracy of the system in the atomic limit.

Finally, let us point out that our perturbative solution at finite order can only yield discrete spectral weight,

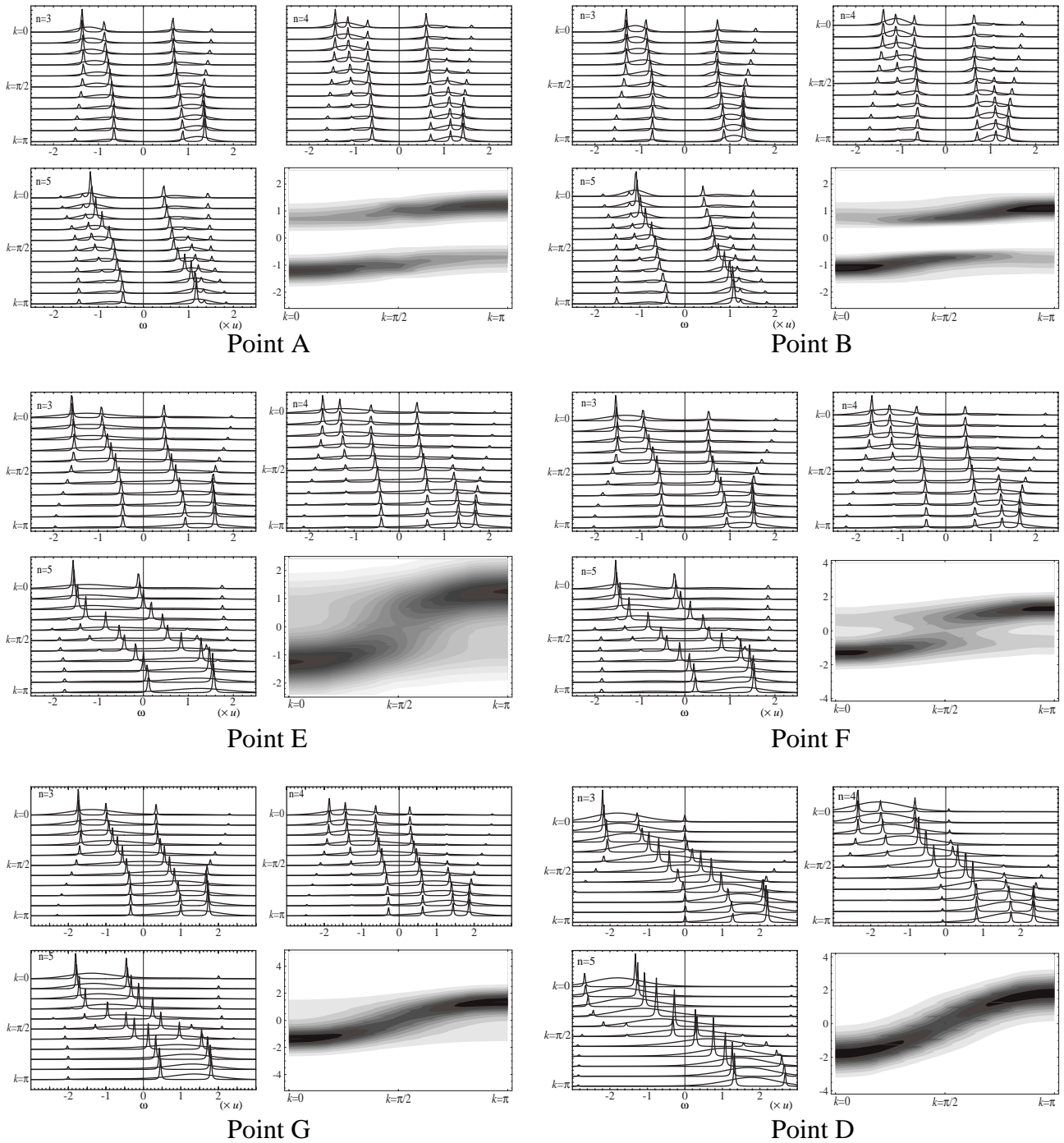


Fig. 5. Spectral weight associated with points A,B,E,F,G and D of the crossover diagrams (Figs. 3 and 7). For each point, we give the spectral weight obtained from order t^3 (top left), t^4 (top right), and t^5 (bottom left). A finite width $\eta = 0.02$ was added for clarity. The Monte-Carlo results [52] (smooth curves) were used to establish the density plot (bottom right). Note that: Point A lies within the insulating paramagnetic region, as can be deduced from the presence of a gap and the monotonous dispersion of the bottom of the upper band (see text for details). For these values of the parameters, order t^4 seems the best approximation. Point B is in the antiferromagnetically correlated region: The minimum in the dispersion of the bottom of the band has shifted to $k > 0$. Orders t^3 and t^4 are best suited there. Point E is in the insulating paramagnetic region and is best described by the fourth-order result. Point F is just at the edge of the antiferromagnetically correlated region. The third-order approximation is the best one. Point G is in the metallic region. Only order t^5 gives the closure of the gap for this point. Point D is well within the metallic region.

whereas the exact solution in the thermodynamic limit certainly has a continuous distribution of poles on the real axis. Such a continuous distribution is in general necessary to account for spin-charge separation, or a finite lifetime of one-particle excitations. Therefore, an approximation describing the spectral weight as a sum of four delta functions is necessarily a crude one. The reason why it is difficult to obtain a continuous spectral weight is the huge degeneracy of the unperturbed Hamiltonian. The starting point being a collection of independent atoms with the same two energy levels, it is not likely that a finite-order perturbation scheme can produce a macroscopic number of distinct approximate eigenvalues. We will discuss in Section 5 a partially self-consistent approach leading to an extended spectral weight. But in the latter case, we no longer have the freedom to add higher-order terms in order to solve the causality problem.

4.3 Comparison with Monte-Carlo data

We now present Monte-Carlo data supporting and illustrating the conclusions claimed so far, regarding the physical behavior of the model, as well as the accuracy of our approximation at various orders in t . The simulations [52] were done for a twenty-site one-dimensional lattice for reasons of computing power and time. The spectral weight was deduced from imaginary time Green functions by the maximum entropy method [53]. The first interesting region is the crossover between the ordinary paramagnetic insulator and the strongly AF correlated insulator. Figure 5 shows the spectral weight for the points A ($t = 0.25u, T = 0.25$) and B ($t = 0.25u, T = 0.125$) on each side of the crossover (Points A to G are indicated in Figs. 3 and 7). Third-, fourth-, and fifth-order results are displayed. Of course, A and B being very close to each other, they have largely similar spectral weights, but their qualitative difference defined in Section 3.3 is supported by the density plot. The fact that orders t^3 and t^4 are equally well suited for these two points, located respectively on the lines $T = t$ and $T = t/2$, is consistent with our argument that order t^5 deteriorates compared to order t^3 precisely in that region. Let us mention that in one dimension, the Monte-Carlo data show that the antiferromagnetically correlated region is tiny, and that a spectral function reminiscent of spin-charge separation (with an important transfer of weight from low to high energy for $k < \pi/2, \omega > 0$ and $k > \pi/2, \omega < 0$) appears when lowering T a little further (actually when entering the shaded area of Fig. 3). However no such thing is expected in two dimensions, for which the antiferromagnetically correlated region extends without spin-charge separation down to $T = 0$ where true long-range order takes place.

The upper border of the paramagnetic insulator region, defined by the closure of the gap, can be computed more precisely than in Figure 3 with the help of the fifth order. It leads to a lower value of t_c , saturating around $t_c \simeq 0.47u$ at high temperature. Order t^5 has been used when establishing the improved crossover diagram of Figure 7. The sequence of points E, G, D, taken along

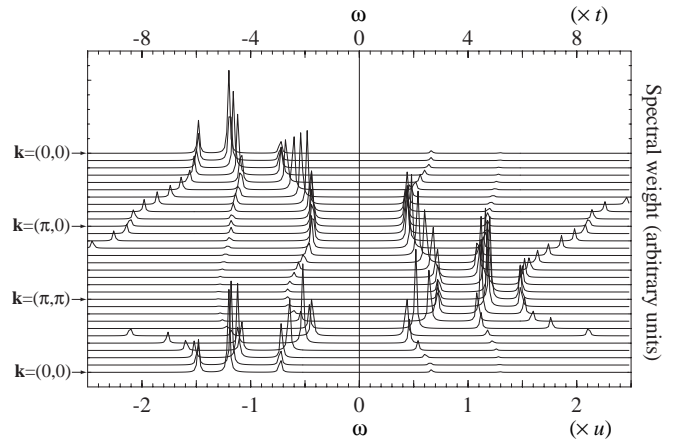


Fig. 6. Spectral weight deduced from our approximate Green function at order t^3 for point H2 of Figure 7 ($t = 0.25u, T = 0.025u$) in dimension $d = 2$. This is to be compared with the Monte-Carlo data of reference [25]. As in dimension $d = 1$ [37], our result agree quite well with the numerical computations despite the low value of the temperature.

the line $T = 1.25t$ for $t = 0.4u, 0.5u, 0.8u$, and also depicted in Figure 5, shows that the gap actually closes for a smaller value of t than predicted by order 3. When lowering the temperature below t , the fifth-order result quickly deteriorates: it does not yield the antiferromagnetic crossover, and wrongly predicts the crossover to the conducting state for decreasing t when $T \rightarrow 0$. Thus, in Figure 7, we use the third-order result to obtain the antiferromagnetic crossover line at low temperatures, and we switch from order t^3 to order t^5 at the crossing point between the insulator to metal line (at high T) and the antiferromagnetic crossover line (at low T). Therefore, the dashed line of Figure 7 separating the paramagnetic metal (gapless) from an antiferromagnetically correlated insulator (gapped) is conjectural. Anyway, the density plot for point F ($t = 0.4u, T = 0.35$) (Fig. 5) clearly shows the tendency to open a gap upon lowering the temperature.

Finally, Figure 6 shows a comparison of the t^4 solution and the Monte-Carlo data of reference [25] for point H2 in the two-dimensional case. The agreement is excellent, even though the parameters fall in a region where we do not expect our approximation to be good. Such a good agreement with Monte-Carlo data outside of the expected region of validity has also been observed in one dimension [37]. This probably means that the criteria (31) are too stringent. One may instead apply the following *a posteriori* criterion: The approximate spectral distribution is reliable if a large fraction of the weight (say, 90%) falls within $\pm t$ of the original Hubbard bands at $\omega = \pm u$ (this is the case for Fig. 6, as well as for Fig. 3 of Ref. [37]). This softer criterion of reliability probes the overall effect of hopping on the spectral weight, without a detailed analysis of partial numerators and denominators, whose effect on the spectral weight is often far from obvious.

To summarize, let us first mention two limitations of the strong-coupling expansion: (i) one cannot expect to describe faithfully the lineshape of the spectral function and (ii) it is impossible to obtain an accurate result for

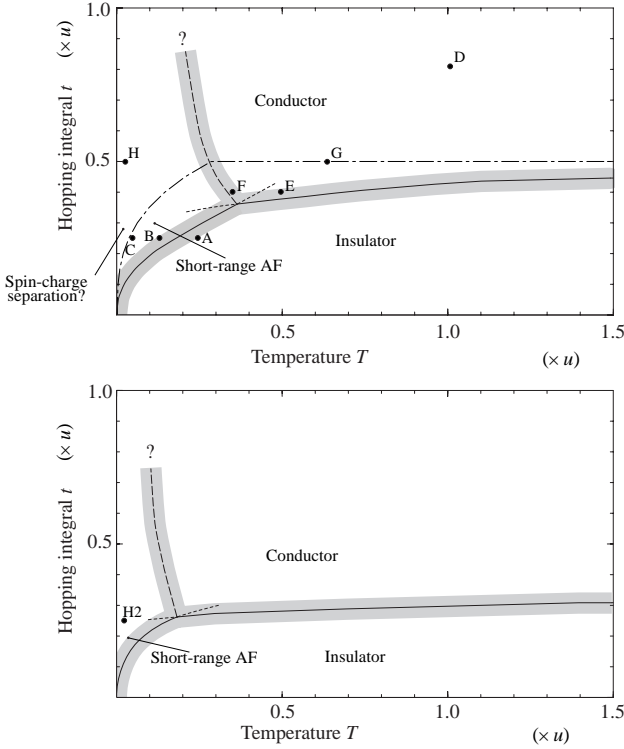


Fig. 7. Improved crossover diagram of the half-filled Hubbard model in dimension $d = 1$ (top) and $d = 2$ (bottom). The dot-dashed line reminds the estimated validity region in one dimension. The antiferromagnetic crossover was calculated with the t^3 order result, and the Mott transition line with the help of order t^5 . The limit between the metallic and the insulating antiferromagnetic regions is no longer clearly defined.

any temperature much lower than t . We add that going beyond fifth order within the systematic approach described in this paper would be difficult and unpractical, since the (intractable) result would be relevant only deep in the insulating region. On the positive side, Monte-Carlo calculations agree well with our results as far as the overall distribution of the weight is concerned. In particular, the fifth order calculation has led to a reliable prediction for the Mott conductor-insulator crossover shown in Figure 7.

4.4 Double occupancy

The double occupancy $\langle n_{\uparrow}n_{\downarrow} \rangle$ is a local static quantity essential to the comprehension of the Hubbard model, which gives in particular the average potential energy $U\langle n_{\uparrow}n_{\downarrow} \rangle$. Exact values of $\langle n_{\uparrow}n_{\downarrow} \rangle$ in dimensions higher than one can be obtained only by numerical methods [23, 55]. It is possible to deduce it from the one-particle Green function through the exact relation:

$$\frac{1}{\beta L^d} \sum_{\mathbf{k}, i\omega} \mathcal{G}_{\sigma}(\mathbf{k}, i\omega) \Sigma_{\sigma}(\mathbf{k}, i\omega) e^{i0^+} = U \langle n_{\uparrow}n_{\downarrow} \rangle, \quad (32)$$

where $\Sigma_{\sigma}(\mathbf{k}, i\omega)$ is the self-energy. There are two possible ways for us to use the identity (32). On the one hand, from our knowledge of the thermodynamic potential Ω (*cf.* Sect. 6 below), we may extract the power series in

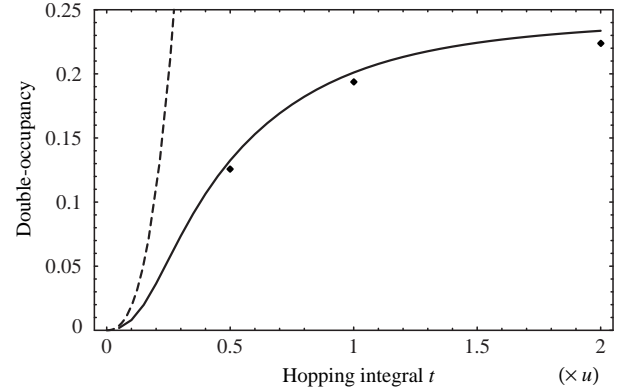


Fig. 8. Double occupancy $\langle n_{\uparrow}n_{\downarrow} \rangle$ as a function of the hopping parameter along the line $T = t/6$ in dimension $d = 2$. Comparison between s_t (dashed), s_J (solid), and Monte-Carlo results [23] (diamonds, bigger than the uncertainty). Both s_t and s_J are calculated at order t^4 .

t (thereafter denoted s_t) of $\langle n_{\uparrow}n_{\downarrow} \rangle$: $\beta s_t = -d\Omega/dU$. On the other hand we can insert the continued fraction (27) into equation (32) and compute $\langle n_{\uparrow}n_{\downarrow} \rangle$ numerically. This subsection shows that the second option (thereafter denoted s_J) gives much better results, which confirms that the continued fraction representation is a controlled way of resumming diagrams. At half-filling, the power series for the double occupancy is:

$$\begin{aligned} s_t &= \frac{1}{1 + e^{\beta}} \\ &+ d \left(\frac{\beta^2 e^{\beta} (-1 + e^{\beta})}{(1 + e^{\beta})^3} - \frac{\beta e^{\beta}}{(1 + e^{\beta})^2} + \frac{-1 + e^{\beta}}{2(1 + e^{\beta})} \right) t^2 \\ &+ d \left(\frac{9(-5 + d)(-1 + e^{\beta})}{32(1 + e^{\beta})} + \beta \frac{3(4 + 7e^{\beta} - 3de^{\beta} + 4e^{2\beta})}{16(1 + e^{\beta})^2} \right. \\ &\quad \left. - 3\beta^2 \frac{(1 + 7d)e^{\beta}(-1 + e^{\beta})}{16(1 + e^{\beta})^3} \right. \\ &\quad \left. - \beta^3 \frac{3(-1 + 3d)e^{\beta}(1 - 4e^{\beta} + e^{2\beta})}{8(1 + e^{\beta})^4} \right. \\ &\quad \left. + \beta^4 \frac{(-3 + 7d)e^{\beta}(-1 + e^{\beta})(1 - 10e^{\beta} + e^{2\beta})}{16(1 + e^{\beta})^5} \right) t^4 + O(t^6), \end{aligned} \quad (33)$$

where we have set $u = 1$. Figure 8 sketches s_t and s_J as functions of t along the line $T = t/6$ in the two-dimensional case, as well as some Monte-Carlo data [23, 55]. Whereas s_t quickly increases beyond the maximum physically acceptable value of $1/4$, s_J interpolates quite well between the low t regime and the high t regime where the form of the continued fraction ensures that the free-particle limit $\langle n_{\uparrow}n_{\downarrow} \rangle \rightarrow 1/4$ is properly recovered. The effect of temperature on double occupancy is summarized in Figure 9, showing s_J as a function of T for several values of t , as well as Monte-Carlo results from references [23, 55].

s_J always presents a minimum at some temperature, which may be more or less sharp. In infinite dimension [54], such a minimum is absent at strong coupling, but appears at moderate and weak coupling, where it

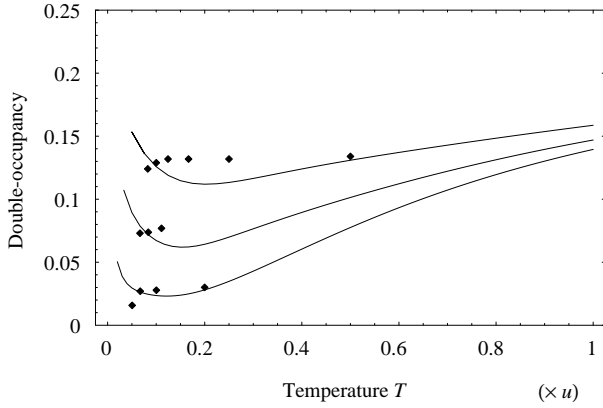


Fig. 9. Double occupancy $\langle n_{\uparrow}n_{\downarrow} \rangle$, computed from s_J at order t^4 , for $d=2$ as a function of temperature for various values of t ($t=0.5u$, $t=0.33u$, $t=0.2u$ from upper to lower curve). The diamonds represent Monte-Carlo results [55].

is explained by a Pomeranchuk effect. A recent application of a two-particle self-consistent approach [56] shows that this minimum is still present in dimension three, but disappears in dimension two: In low dimensions the self-energy acquires a momentum dependence that makes it more sensitive to magnetic correlations, thus suppressing the Pomeranchuk effect. In any case, we believe that this minimum in s_J is an artifact of our approximation, not an entropy effect. Indeed, when lowering T well below that minimum, we enter the regime where the self-energy artificially goes to zero with temperature, and consequently the double occupancy goes to $1/4$. We have stressed several times that this limit is not well-rendered by our solution, and it is confirmed by Monte-Carlo data which show little T dependence at low T . Anyway, as long as we stay in the vicinity of this artificial minimum, our theoretical predictions differ from the Monte-Carlo values by at most 15% for $t=0.5u$ ($U=4t$), and the agreement improves quickly at high temperatures, even for values of U in the intermediate coupling regime, as in Figures 8 and 9. It is expected that the agreement will be better in higher dimension. Moreover, at low temperature, the agreement is better for smaller values of t/u , as expected.

5 Infinite resummations

Up to now, we have followed a systematic approach, which consists in building the series in powers of t of a given quantity. This has led us to interesting results, but has also shown its limits: (i) it does not yield continuous spectral functions and (ii) we have pushed the calculations to their maximum acceptable complexity level. At this point, rather than keeping all diagrams of a given order, we look for infinite series of diagrams that might embody an interesting physical feature of the model.

5.1 RPA-like propagator

The most natural possibility is to resume all the “rosary” diagrams, that is, to replace the auxiliary fermion

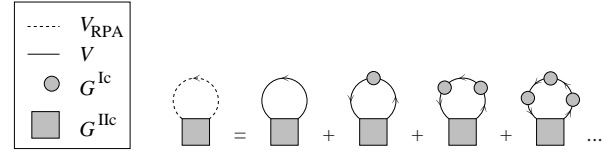


Fig. 10. The one-loop “rosary” diagram. The simple hopping term is replaced by an RPA-like propagator.

propagator $V(\mathbf{k})$ by

$$\frac{V(\mathbf{k})}{1 - V(\mathbf{k})G(i\omega)} \quad (34)$$

wherever it appears in the diagrams. This prescription corresponds to an alternate way of separating free and interacting parts of the action, as mentioned at the end of Section 2.2. With this new propagator, the electron, instead of simply hopping between two neighboring sites, can travel an arbitrary sequence of one hop (of amplitude $V(\mathbf{k})$) followed by a period of rest on some site (of amplitude $G(i\omega)$). The simplest series of this kind is shown in Figure 10. The result in $d=1$ is:

$$\Gamma(i\omega) = \frac{i\omega}{(i\omega)^2 - u^2} + \frac{3u^2}{i\omega((i\omega)^2 - u^2)} \times \left(-1 + \frac{1}{\sqrt{1 - \left(\frac{2ti\omega}{(i\omega)^2 - u^2}\right)^2}} \right). \quad (35)$$

Let us comment on $\Gamma(i\omega)$, which coincides with the entire Green function when $k = \pi/2$. Our main objective has been fulfilled, in the sense that the spectral weight $A(\pi/2, \omega)$ is now a continuous distribution in the band

$$-t + \sqrt{t^2 + u^2} < \omega < t + \sqrt{t^2 + u^2} \quad (36)$$

and is symmetric. On the other hand, $A(\pi/2, \omega)$ is not everywhere positive. Indeed, a detailed analytic study of $\Gamma(i\omega)$ shows that it has a positive spectral weight everywhere except at $\omega = \pm u$. At those points, the first term of equation (35) brings a delta function of weight $1/2$, and the second term a delta function of weight $-3/2$, resulting in a negative peak in the spectral weight. The prefactor 3 in front of the second term has been thoroughly checked, and we have achieved great confidence that equation (35) is correct. When $k \neq \pi/2$, the spectral weight has to be derived from the imaginary part of

$$\mathcal{G}(k, i\omega) = \frac{1}{\Gamma(i\omega)^{-1} + 2t \cos(k)} \quad (37)$$

when $i\omega \rightarrow \omega + i\eta$. Like for $k = \pi/2$, $A(k, \omega)$ is nonzero within the bands, and negative at $\omega = \pm u$. In addition, $A(k, \omega)$ has two delta peaks near the edges of, and outside the bands – where the Green function has no imaginary part. Figure 11 shows $A(0.5\pi, \omega)$ and $A(0.4\pi, \omega)$ for $t=0.5u$.

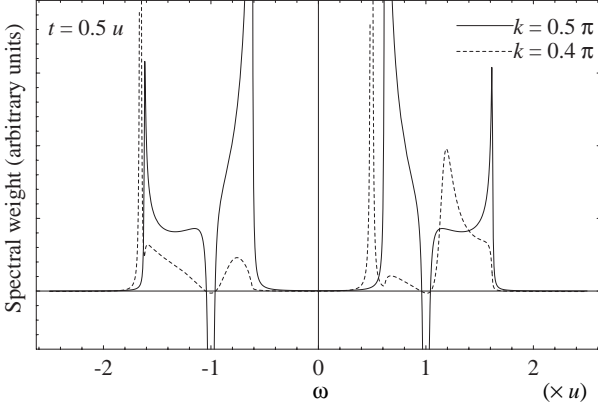


Fig. 11. Spectral weight obtained with the auxiliary self-energy of Figure 10, with hopping term $t = 0.5u$, and momentum $k = 0.5\pi$ (full curve) and $k = 0.4\pi$ (dashed curve). The spectral weight is not everywhere positive within this approximation.

Thus, the one-loop diagram of leads to a normalized, but nonpositive spectral weight. We have also lost the interesting physical effects of order three: the result is temperature-independent and always has a gap at the Fermi level. We did not find any acceptable way to cure this negative-weight problem. One could suggest to reduce the normalization of the one-loop diagram of Figure 10, but introducing such an arbitrary factor is by no means justified.

5.2 One-loop self-consistent approximation

Another natural attempt involving an infinite subset of diagrams is to compute the one-loop self-consistent solution: We keep the first two diagrams of Figure 2, and discard all vertices beyond G^{IIc} . The self-consistent solution $\tilde{\Gamma}(i\omega)$ obeys the following equation:

$$\tilde{\Gamma}_\sigma(i\omega) = G_\sigma(i\omega) - \frac{1}{\beta L^d} \sum_{\sigma_1, \mathbf{k}_1, i\omega_1} G_{\sigma, \sigma_1; \sigma, \sigma_1}^{\text{IIc}}(i\omega, i\omega_1; i\omega, i\omega_1) \times \frac{V(\mathbf{k}_1)}{1 - V(\mathbf{k}_1)\tilde{\Gamma}(i\omega_1)}. \quad (38)$$

The sum in equation (38) can be computed exactly, given the following property of G^{IIc} at half filling and zero magnetic field:

$$\sum_{\sigma_1} G_{\sigma, \sigma_1; \sigma, \sigma_1}^{\text{IIc}}(i\omega, i\omega_1; i\omega, i\omega_1) = \frac{-3\beta u^2 \delta(i\omega - i\omega_1)}{((i\omega)^2 - u^2)^2} + \mathcal{E}(i\omega, i\omega_1), \quad (39)$$

where \mathcal{E} is an even function of $i\omega_1$. Since we expect $\tilde{\Gamma}_\sigma(i\omega)$ to be antisymmetric in $i\omega$, the self-consistent propagator in equation (38) is antisymmetric when $i\omega_1 \rightarrow -i\omega_1$ and

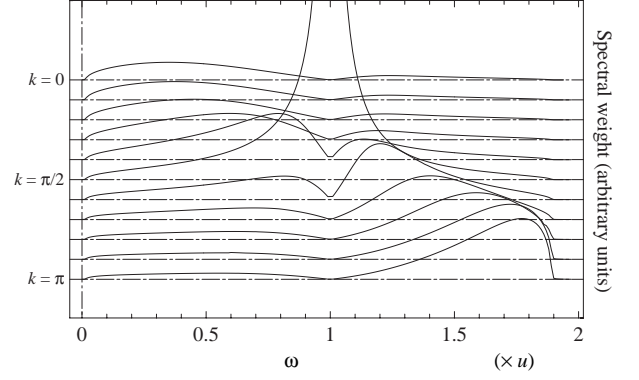


Fig. 12. Spectral weight of the one-loop self-consistent solution, for $t = t_c = 0.39u$. The wavevector goes from $k = 0$ (top) to $k = \pi$ (bottom). The spectral function is clearly not normalized within this approximation.

$\mathbf{k}_1 \rightarrow (\pi, \dots, \pi) - \mathbf{k}_1$. Therefore, \mathcal{E} does not contribute and

$$\tilde{\Gamma}_\sigma(i\omega) = G_\sigma(i\omega) + \frac{3u^2}{((i\omega)^2 - u^2)^2} \frac{1}{L^d} \times \sum_{\mathbf{k}_1} \frac{V(\mathbf{k}_1)}{1 - V(\mathbf{k}_1)\tilde{\Gamma}(i\omega)}. \quad (40)$$

Equation (40) can easily be solved numerically. Among the various solutions for the spectral weight, we retain the positive one having a compact support at very small t , and follow its evolution when increasing t . The result is shown in Figure 12 for $t = 0.25u$, and is obviously not normalized. The quick suppression of spectral weight close to $\omega = \pm u$ when k differs slightly from $\pi/2$ is a surprising feature too. However, we have recovered the closure of the gap for $t \simeq 0.39u$, a value close to the prediction of order t^5 at high temperature.

The two examples just described show that it is not easy to include self-consistency in strong-coupling perturbation theory. Lack of positivity or normalization appears in the simplest attempts, and there is no clue on how to solve this problem. However, it seems the only way of obtaining a continuous spectral function, and further developments should probably include a dose of self-consistency.

6 Doping

Studying the Hubbard model at arbitrary filling is important for several reasons. First of all, the charge gap of the half-filled system disappears upon doping, and in dimension $d = 1$, bosonization shows that this implies dramatic changes in the spectral weight. Furthermore, in dimension $d = 2$, a slight doping is directly relevant to the high- T_c superconductors. Finally, the metal-insulator transition can be induced by doping rather than by interactions. We address the latter aspect in this section.

On technical grounds, working with arbitrary chemical potential is extremely difficult, since the complete expression of G^{IIc} given in Appendix B is already hardly

tractable, and using it to compute diagrams would be even worse. Even if it is obviously preferable to include the full atomic Green function in the unperturbed part, one could treat the shift in chemical potential $t_0 = \mu - u$ as a perturbation, as is done in Appendix C. However, the spatial integrals would no longer cancel several low-order diagrams involving G^{IIIc} and G^{IVc} . Hence the calculation was carried out with a given μ , without expanding it as $\mu = u + t_0$, with the help of a suitable generalization of our special purpose symbolic manipulation program. We were able to compute Γ up to order t^3 in dimension $d = 1$, and to build the corresponding continued fraction. The partial numerators and denominators of the latter are given in equations (41, 42) below.

$$\begin{aligned} a_0 &= 1 \\ a_1 &= -4u \left[-2\beta(1-2\nu)^2(\nu^2 - \nu_2)t^2 + (-1 + \nu)\nu u \right. \\ &\quad \left. + \beta^2(1-2\nu)^2 \times (-\nu + 4\nu^2 + \nu_2 - 8\nu\nu_2 + 4\nu_2^2)t^2 u \right] \\ a_2 &= 6t^2 + \frac{4\beta \cos(k)(-1+2\nu)(\nu - \nu_2)t^3}{(-1 + \nu)\nu} \\ a_3 &= \frac{-4(-2 - \nu + \nu^2)u^2}{9} \\ &\quad - \frac{8\beta \cos(k)(-1+2\nu)^3(\nu - \nu_2)tu^2}{27(-1 + \nu)\nu} \end{aligned} \quad (41)$$

$$\begin{aligned} b_1 &= -2t \cos(k) + t_0 - (-1 + 2\nu) \left[4\beta(-\nu^2 + \nu_2)t^2 \right. \\ &\quad \left. + u + 2\beta^2(-\nu + 4\nu^2 + \nu_2 - 8\nu\nu_2 + 4\nu_2^2)t^2 u \right] \\ b_2 &= t_0 + (-1 + 2\nu)u + \frac{2\beta(-1 + 2\nu)t^2}{(-1 + \nu)\nu} \\ &\quad \times \left\{ \nu_2 + \nu^4(-2 + 4\beta u) + \nu^3(2 - \beta(5 + 8\nu_2)u) \right. \\ &\quad \left. - \nu(1 + 4\beta\nu_2^2 u + \nu_2(2 + \beta u)) \right. \\ &\quad \left. + \nu^2(\beta u + 4\beta\nu_2^2 u + \nu_2(2 + 9\beta u)) \right\} \\ &\quad + \frac{2\beta \cos(k)t^3}{(-1 + \nu)\nu u} \left\{ \nu^4(-2 + 4\beta u) + \nu_2(-1 + \beta\nu_2 u) \right. \\ &\quad \left. + \nu^2(1 + \beta u + 4\beta\nu_2^2 u + 2\nu_2(1 + 4\beta u)) \right. \\ &\quad \left. - 2\nu\nu_2(1 + \beta(u + 2\nu_2 u)) - 2\nu^3(-1 + 2\beta(u + 2\nu_2 u)) \right\} \\ b_3 &= \frac{3t_0 + u - 2\nu u}{3} + \frac{2 \cos(k)t}{9(-1 + \nu)\nu} \\ &\quad \times \left\{ 2\beta\nu_2 u + \nu^2(-9 + 8\beta(1 + \nu_2)u) - 8\beta\nu^3 u \right. \\ &\quad \left. + \nu(9 - 2\beta(u + 4\nu_2 u)) \right\} \\ b_4 &= t_0 + \frac{(-1 + 2\nu)u}{3} + \frac{\cos(k)t}{9(-1 + \nu)\nu} \\ &\quad \times \left\{ -4\beta\nu_2 u + \nu^2(9 - 16\beta(1 + \nu_2)u) + 16\beta\nu^3 u \right. \\ &\quad \left. + \nu(-9 + 4\beta(u + 4\nu_2 u)) \right\}, \end{aligned} \quad (42)$$

where

$$\nu = \frac{e^{2\beta t_0} + e^{\beta(t_0+u)}}{1 + e^{2\beta t_0} + 2e^{\beta(t_0+u)}} \quad (43)$$

is the average number of electrons of a given spin per site in the atomic limit, and

$$\nu_2 = \frac{e^{2\beta t_0}}{1 + e^{2\beta t_0} + 2e^{\beta(t_0+u)}} \quad (44)$$

the double occupancy in the atomic limit. Although complicated, equations (41, 42) are plausible for several reasons. First, our symbolic manipulation program was checked on the thermodynamic potential, and our result agree with references [33, 34], indicating again that the result of reference [32] is incorrect. Secondly, the half-filling case is properly recovered from equations (41, 42).

At high-enough temperature, the spectral weight derived from equations (41, 42) evolves smoothly with the chemical potential. For example, for $0 < t_0 \ll u$, the Fermi level shifts slightly towards the positive energy peaks, whereas the weight of the latter increases slightly, with respect to the half-filled case. A similar conclusion applies to the density of states: increasing μ shifts the Fermi level towards the upper Hubbard band, and gives the latter more weight, the overall effect being an increase in the occupation number. In other words, except for the expected redistribution of weight [57], the behavior of the system resembles that of a band insulator.

However, this smooth picture collapses when the temperature is too low, the spectral weight abruptly becoming negative at various energies, which means that the a_i 's of equation (25) are no longer all positive. This is yet another manifestation of the limitation of our method at low temperature where, according to references [24, 25], there should be a quick and massive redistribution of spectral weight between the Hubbard bands when varying μ . The breakdown of our solution, which occurs around $T \simeq t$, is concomitant with a lack of monotonicity in the relation between chemical potential and filling. This relation is implicitly defined by the thermodynamical potential through the relation

$$n = -\frac{\partial \Omega}{\partial \mu}, \quad (45)$$

and becomes ambiguous as soon as the thermodynamical potential is only known approximately. From this expression a truncated power series in t for n (denoted $n^{(r)}(\mu)$ at order t^r) follows directly. Alternately, one may reverse this relation and express μ as a truncated power series in t , which we write $\mu^{(r)}(n)$. The two expansions $n^{(r)}(\mu)$ and $\mu^{(r)}(n)$ may lead to different physical conclusions, which would be unacceptable. We have verified that, when lowering the temperature, both functions $n^{(2)}(\mu)$ and $\mu^{(2)}(n)$, calculated at order t^2 , cease to be monotonous nearly at the same value of T/t , which is also the temperature at which the spectral weight becomes unphysical.

Nonetheless, and similarly to what we did in the half-filled case, we can use the penetration of the Fermi level into one of the Hubbard bands as a qualitative criterion for the metal-insulator crossover. This penetration should translate into an important increase of occupied states (likely to be delocalized) in either Hubbard band, and therefore an increase in the conductivity. Figure 13 shows,

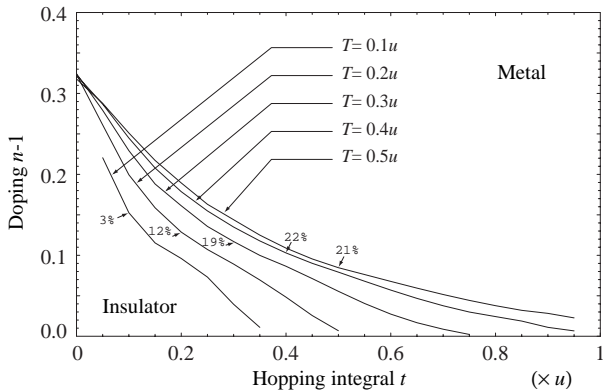


Fig. 13. Location of the metal-insulator crossover at various temperatures. The numbers are estimations of the relative error on $n-1$ at the points $t = T$, given that the solution quickly breaks down for $t > T$.

for several temperatures, the line in the $(t, n-1)$ -plane where the Fermi level enters the upper Hubbard band. The numbers associated with each curve are estimations of the accuracy at the points $T = t$, beyond which the solution breaks down. These numbers are the relative difference between the results for $n(\mu)$ obtained in two independent ways: from the Green function (through the density of states) and from the thermodynamical potential.

Note from Figure 13 that, in the atomic limit $t \rightarrow 0$, the transition occurs near $n-1 = \frac{1}{3}$. Indeed, in the atomic limit, it is a simple matter to show that the chemical potential vanishes at $T = 0$ at this filling, and finite temperature corrections are exponentially small as long as $T \lesssim u$. The chemical potential then touches one of the (infinitely narrow) atomic bands (at $\omega = 0$ and $\omega = 2u$) and any infinitesimal value of t makes the system conduct.

Thus, in the high-temperature regime where our method is reliable, the Mott-Hubbard insulator shares some of the features of a band insulator: the gap is nearly rigid, and a crossover towards a good conductivity is obtained when the population of carriers ceases to be exponentially small. In contrast to a band insulator, there is, however, some transfer of spectral weight towards the band closest to the Fermi level, when μ is changed from its half-filled value.

For $T < t$, the expected drastic changes in the spectral weight are not properly described by our approximate solution, which instead becomes unphysical.

7 Conclusion

In this work, we have pushed the strong-coupling expansion [37] of the single-particle spectral weight to higher order and checked the accuracy of the results by detailed comparisons with Monte Carlo simulations. Among our main results are the crossover diagrams of Figure 7. They demonstrate the possibility of describing the three qualitatively different regions of parameter space of the half-filled Hubbard model by a single perturbative expression for

the Green function. The importance of higher order terms is revealed, for example, by point G in Figure 5 that would be wrongly assigned to the insulating phase if only third order results [37] were used. An important physical consequence of our results is that $A(\mathbf{k}, \omega)$ depends strongly on temperature, as illustrated by the difference between our spectral weights (both perturbation expansion and simulations) and their zero-temperature counterparts obtained from other methods. We have also shown that calculations may be performed away from half-filling, leading to a metal-insulator crossover diagram as a function of temperature, doping and interaction strength (Fig. 13). Double occupancy is also a quantity that may be computed from single-particle quantities. By comparing the results with Monte Carlo simulations (Figs. 8 and 9) we have demonstrated again the value of the continued-fraction (Lehmann) representation.

An important difficulty of any expansion about the atomic limit is the absence of Wick theorem for the atomic limit itself. The auxiliary fermions allowed us to organize the expansion in the best possible way, and to reduce tremendously the number of diagrams at a given order. Nevertheless, the exact G^{Rc} 's are still necessary, and the result of Appendix B for G^{Ic} suggests that they are quite difficult to compute for $R \geq 3$. Introducing a physically motivated approximation scheme for the atomic vertices would allow further progress, particularly on the two-particle correlation functions. The full two-particle correlation function in the atomic limit ($U \rightarrow \infty$, Appendix B) is a noteworthy byproduct of our work.

Perturbation series for interacting electrons are by nature asymptotic. We have also discussed in detail and in various contexts the subtleties involved when the series is pushed to higher order. In an expansion in powers of t , one should assume that, however the series is resumed, there are two dimensionless expansion parameters, t/u and t/T . Hence, roughly speaking, even for small t/u , when the temperature is low, ($T < t$) the series breaks down and higher-order terms degrade the quality of the solution, while at higher temperature ($T > t$) higher order terms improve it.

The intrinsic limitations of the strong-coupling perturbation series were also pointed out:

1. Even though our method exhibits the effect of antiferromagnetic correlations on single particle properties, as clearly shown for example in Figure 4, it breaks down quickly as temperature is lowered further and magnetic correlations become too strong. However, as long as these correlations play a negligible role, *e.g.* at high-enough temperature, all dimensions are known to show similar behaviors as far as the metal-insulator crossover is concerned, in agreement with the weak dimension dependence of our results (we include dimension $d = 1$, for which the gap predicted by Bethe Ansatz is exponentially small in a finite range of U/t) [58]. Our method fails at lower temperature, where the system evolves towards spin-charge separation ($d = 1$), or a true antiferromagnetic transition at zero ($d = 2$) or finite ($d \geq 3$) temperature.

Nevertheless, the possibility to take into account the effect of antiferromagnetic fluctuations on single-particle properties above the antiferromagnetic transition, is an improvement over $d = \infty$ methods [28].

2. The systematic strong-coupling expansion can only provide a finite number of poles in the continued fraction and the corresponding approximate Green function cannot have continuous spectral weight. This does not prevent meaningful comparisons with Monte-Carlo data, since the overall spectral weight distribution can be assessed. This “discreteness problem” might be solved with the help of a suitable termination function within the continued fraction [59], but this is impossible without any prior knowledge about the Green function. Furthermore, we have shown that the simplest ways of obtaining a continuous spectral weight from infinite subsets of diagrams lead to nonpositive or unnormalized functions. One way of increasing the number of significant poles is to treat a cluster of sites as a single “site” from the point of view of the strong-coupling expansion, and to carry the calculations numerically [60].

The major challenge faced by the strong-coupling perturbation theory is the low-temperature barrier. We pointed out that the exponentially large degeneracy of the atomic ground state is likely to be the source of the problem. One possible solution to this difficulty is to select a ground state more likely to connect with the low-temperature phases and to organize the perturbation series around that ground state, which would imply a certain amount of self-consistency. Work along these lines is in progress.

While this paper focused on properties derived from the one-particle Green function, two-particle Green functions are also accessible within the method presented here, but their systematic computation is more involved at order t^4 (it requires the atomic four-particle function G^{IV}). For this reason, we defer discussion of two-particle correlations to a future publication.

We thank C. Bourbonnais and N. Dupuis for many useful discussions. We are grateful to H. Touchette, S. Moukouri, L. Chen, and especially D. Poulin and S. Allen for sharing their numerical results. Monte Carlo simulations were performed in part on an IBM SP2 at the Centre d’applications du calcul parallèle de l’Université de Sherbrooke. This work was partially supported by NSERC (Canada), by FCAR (Québec) and by a scholarship from MESR (France) to S.P.

Appendix A: Diagrammatic rules

This appendix is devoted to deriving and illustrating the diagrammatic theory valid for the auxiliary field introduced in Section 2.2. For definiteness, we suppose that the site index describes a d -dimensional hypercubic lattice, and we only consider Hamiltonians where the h_i ’s do not explicitly depend on i , so that the interaction terms are translation invariant, in addition to being local in space.

The first step consists in expanding the exponential of the interaction terms of equation (10):

$$Z = \int [d\psi^* d\psi] e^{-S_0[\psi^*, \psi]} \sum_{P=0}^{\infty} \frac{(-)^P}{P!} \left(\sum_{R=1}^{\infty} S_{\text{int}}^R[\psi^*, \psi] \right)^P. \quad (\text{A.1})$$

For a given P , and taking into account the factor $(-)^P/P!$, we have a sum of terms of the following form:

$$\frac{(-)^P}{C_1! \dots C_H!} S_{\text{int}}^{R_1}[\psi^*, \psi] \dots S_{\text{int}}^{R_P}[\psi^*, \psi], \quad (\text{A.2})$$

where R_1, \dots, R_P are P integers, and C_1, \dots, C_H the multiplicities of the different values that occur in the sequence R_1, \dots, R_P . Suppose we are interested in the following correlation function:

$$\mathcal{V}_{a_1^0 \dots a_R^0, b_1^0 \dots b_R^0}^R = (-)^{R_0} \left\langle \psi_{a_1^0} \dots \psi_{a_{R_0}^0} \psi_{b_{R_0}^0}^* \dots \psi_{b_1^0}^* \right\rangle. \quad (\text{A.3})$$

The contribution of a given power P to (A.3) is the sum, for all possible sequences R_1, \dots, R_P , of

$$\begin{aligned} & \frac{Z_{\text{Gauss}}}{Z} \sum_{\substack{\{a_r^p, b_r^p\} \\ p=1 \dots P \\ r=1 \dots R_p}}' G_{\{b_r^1\}\{a_r^1\}}^{R_1 c} \dots G_{\{b_r^P\}\{a_r^P\}}^{R_P c} \left\langle \psi_{a_1^0} \dots \psi_{a_{R_0}^0} \psi_{a_1^1} \dots \psi_{a_{R_1}^1} \right. \\ & \times \left. \dots \psi_{a_1^P} \dots \psi_{a_{R_P}^P} \psi_{b_{R_P}^P}^* \dots \psi_{b_1^P}^* \psi_{b_{R_1}^1}^* \dots \psi_{b_1^1}^* \dots \psi_{b_{R_0}^0}^* \dots \psi_{b_1^0}^* \right\rangle_{\text{Gauss}}, \end{aligned} \quad (\text{A.4})$$

times a overall factor

$$\frac{(-)^{R_0}}{C_1! \dots C_H! (R_1!)^2 \dots (R_P!)^2}, \quad (\text{A.5})$$

which takes into account the minus signs coming with S_{int}^R . Again, let us stress that the indices in the sum do not run over all their possible values, but rather are restricted to have a common site index if they refer to the same vertex (this restriction is encoded in the primed sum). Since the action is Gaussian, Wick’s theorem is valid, and one can compute the average in expression (A.4) as a sum over all possible permutations ϑ of $R_0 + R_1 + \dots + R_P$ elements:

$$\begin{aligned} (\text{A.4}) = & \frac{Z_{\text{Gauss}}}{Z} \sum_{\vartheta} (-)^{\vartheta} \sum_{\substack{\{a_r^p, b_r^p\} \\ p=1 \dots P \\ r=1 \dots R_p}}' G_{\{\vartheta(b_r^1)\}\{a_r^1\}}^{R_1 c} \dots \\ & \left\langle \psi_{a_1^0} \psi_{\vartheta(b_1^0)}^* \right\rangle_{\text{Gauss}} \dots \left\langle \psi_{a_{R_P}^P} \psi_{\vartheta(b_{R_P}^P)}^* \right\rangle_{\text{Gauss}}, \end{aligned} \quad (\text{A.6})$$

where $(-)^{\vartheta}$ stands for the signature of the permutation, and $\langle \psi_{a_i^j} \psi_{\vartheta(b_i^j)}^* \rangle_{\text{Gauss}} = -V_{a_i^j \vartheta(b_i^j)}$. A term in the sumover

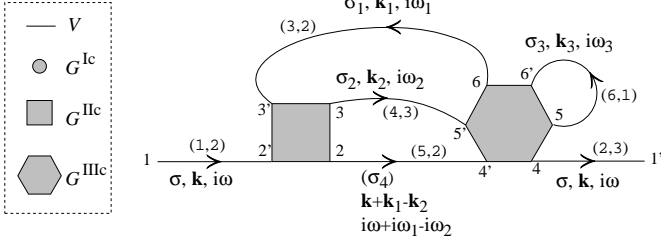


Fig. 14. Diagram of order $|V|^6$ contributing to the Green function of the auxiliary field $\mathcal{V}_\sigma(\mathbf{k}, i\omega)$.

the permutations can be represented easily by a Feynman diagram, according to the following rules:

1. Draw P polygons (vertices) having $2R_1, \dots, 2R_P$ apices (internal points) respectively, and $2R_0$ isolated points (external points).
2. To half of the external points and half of the apices of each vertex, attach an outgoing arrow (a “bra”, corresponding to a ψ). To the rest of the points and apices, attach an incoming arrow (a “ket”, corresponding to a ψ^*).
3. Label the bras in a conventional order (first the external ones, then all the bras of each vertex consecutively), and label the kets with corresponding primed integers.
4. To each point assign a Latin index, the indices of the internal points sharing the same value of the spatial component for each vertex.
5. Finish drawing the arrows according to the permutation ϑ . To the lines assign a propagator V_{ab} (bra index first), and to the vertices assign a $G_{\{b_r^P\}\{a_r^P\}}^{R_P c}$ (ket indices first).
6. Integrate over all the internal variables.

A few remarks are in order. First, the ratio Z_{Gauss}/Z allows a restriction to connected diagrams only [61]. Secondly, it can easily be seen that the exchange of two equivalent vertices does not change the value of a diagram, nor does the exchange of two internal points of the same type (bra or ket) on the same vertex. This allows a restriction to topologically different diagrams, each of which with a proper multiplicity factor. Thus, to span all the permutations, it is sufficient to consider only the topologically distinct diagrams, and to assign them a factor

$$\frac{(-)^{R_1+\dots+R_P+\vartheta} \times \text{multiplicity}}{C_1! \dots C_H! (R_1!)^2 \dots (R_P!)^2}. \quad (\text{A.7})$$

Due to the presence of various types of vertices (n -body interaction, $n = 1, 2, \dots$), the counting of the sign and symmetry factor cannot be simplified as in the usual two-body interaction case. A third remark is that in general \mathcal{H}^0 and \mathcal{H}^1 conserve spin, and so spin is conserved along the lines, and the total spin entering a vertex is the same as the total spin leaving it.

After a Fourier transform, space and time translation invariance of the on-site Hamiltonian h result in the conservation of total momentum and total Matsubara frequency at each vertex. The rules remain the same, except that one can *a priori* impose the above conservation laws along the lines and at each vertex. There remain $R_1 + \dots + R_P - R_0 - P + 1$ independent internal variables entering sums of the following type:

$$\frac{1}{\beta L^d} \sum_{\sigma, \mathbf{k}, ik_n} \dots, \quad (\text{A.8})$$

where L is the size of the lattice, \mathbf{k} a vector of the reciprocal lattice, and $ik_n = i(2n+1)\pi T$ a fermionic Matsubara frequency. Finally, if the on-site Hamiltonian h is sufficiently simple as to allow for an exact computation of the vertices (the G^{Rc} 's), we can obtain, by usual diagrammatic perturbation theory, any correlation function of the auxiliary field. We still have to derive from them the electron correlation functions: this is done in Section 2.3. Figure 14 shows an example of a diagram of order 6 contributing to $\mathcal{V}_{ab} = -\langle \psi_a \psi_b^* \rangle$. The algebraic expression corresponding to Figure 14 is

$$\begin{aligned} S \sum_{\sigma_1, \sigma_2, \sigma_3} \frac{V(\mathbf{k})^2}{(\beta L^d)^4} \\ \times \sum_{\substack{\mathbf{k}_1, \mathbf{k}_2, \mathbf{k}_3 \\ i\omega_1, i\omega_2, i\omega_3}} V(\mathbf{k}_1) V(\mathbf{k}_2) V(\mathbf{k}_3) V(\mathbf{k} + \mathbf{k}_1 - \mathbf{k}_2) \\ \times G_{\sigma, \sigma_1; (\sigma_4), \sigma_2}^{\text{IIc}}(i\omega, i\omega_1; i\omega + i\omega_1 - i\omega_2, i\omega_2) \\ \times G_{(\sigma_4), \sigma_2, \sigma_3; \sigma, \sigma_3, \sigma_1}^{\text{IIIc}}(i\omega + i\omega_1 - i\omega_2, i\omega_2, i\omega_3; i\omega, i\omega_3, i\omega_1), \end{aligned} \quad (\text{A.9})$$

where S is the symmetry and sign factor. The value of σ_4 can always be inferred from that of the other spins. In the present case, $R_1 + R_2 = 2 + 3 = 5$, so the global sign is opposite to that of the permutation between the unprimed and the primed indices: -1 . The symmetry factor is determined by the numbers between parentheses: the first one is the order in which the lines were drawn, and the second one the number of equivalent possibilities of drawing them. The result is

$$S = -\frac{2 \times 3 \times 3 \times 2 \times 1 \times 1}{(1!)(1!)(2!)^2(3!)^2} = -\frac{1}{4}. \quad (\text{A.10})$$

The rules for the thermodynamic potential are nearly the same. From equation (8) one has

$$\Omega = \Omega_0 - T \log \int [d\psi^* d\psi] e^{\langle \psi | V^{-1} | \psi \rangle} \left\langle e^{\langle \psi | \gamma \rangle + \langle \gamma | \psi \rangle} \right\rangle_0. \quad (\text{A.11})$$

We know Ω_0 exactly, and the second term is obtained by the sum of all connected diagrams with no external points,

times $-T$. If we consider the thermodynamic potential per site, the factor becomes $-1/(\beta L^d)$. When computing the diagrams in momentum space, the factor $1/(\beta L^d)$ is already taken into account by the definition of the various Fourier transforms. Figure 15 shows a diagram contributing to the thermodynamic potential at order 4. The algebraic expression corresponding to Figure 15 is

$$\begin{aligned}
S & \sum_{\sigma_1, \sigma_2, \sigma_3} \frac{1}{(\beta L^d)^3} \sum_{\substack{\mathbf{k}_1, \mathbf{k}_2, \mathbf{k}_3 \\ i\omega_1, i\omega_2, i\omega_3}} V(\mathbf{k}_1)V(\mathbf{k}_2)V(\mathbf{k}_3)V(\mathbf{k}_1 + \mathbf{k}_2 - \mathbf{k}_3) \\
& \times G_{\sigma_1, \sigma_2; \sigma_3, (\sigma_4)}^{\text{IIC}}(i\omega_1, i\omega_2; i\omega_3, i\omega_1 + i\omega_2 - i\omega_3) \\
& \times G_{\sigma_3, (\sigma_4); \sigma_1, \sigma_2}^{\text{IIC}}(i\omega_3, i\omega_1 + i\omega_2 - i\omega_3; i\omega_1, i\omega_2). \tag{A.12}
\end{aligned}$$

Here, $R_1 + R_2 = 2 + 2 = 4$, so the global sign is opposite (see Eq. (A.11) and the following paragraph) to that of the permutation between the unprimed and the primed indices: -1 . The symmetry factor is

$$S = -\frac{2 \times 1 \times 2 \times 1}{(2!)(2!)^2(2!)^2} = -\frac{1}{8}. \tag{A.13}$$

Appendix B: Atomic correlation functions

This appendix gives the one-particle and two-particle correlation functions of the atomic limit of the Hubbard model. The chemical potential is μ and there is a uniform magnetic field h .

$$\mathcal{H}_{\text{at}} = U c_{\uparrow}^{\dagger} c_{\downarrow}^{\dagger} c_{\downarrow} c_{\uparrow} - \mu(c_{\uparrow}^{\dagger} c_{\uparrow} + c_{\downarrow}^{\dagger} c_{\downarrow}) - h(c_{\uparrow}^{\dagger} c_{\uparrow} - c_{\downarrow}^{\dagger} c_{\downarrow}). \tag{B.1}$$

B.1 Green function

The Green function

$$G_{\sigma}(\tau_1, \tau_2) = -\langle T_{\tau} c_{\sigma}(\tau_1) c_{\sigma}^{\dagger}(\tau_2) \rangle \tag{B.2}$$

is straightforward to obtain. Introducing the mean occupation for each spin

$$n_{\pm} = \frac{e^{(\mu \pm h)\beta} + e^{(2\mu - U)\beta}}{1 + e^{(\mu + h)\beta} + e^{(\mu - h)\beta} + e^{(2\mu - U)\beta}}, \tag{B.3}$$

the Fourier transform of the Green function reads:

$$G_{\pm}(i\omega) = \frac{1 - n_{\mp}}{i\omega + \mu \pm h} + \frac{n_{\mp}}{i\omega + \mu \pm h - U} \quad (\sigma = \pm). \tag{B.4}$$

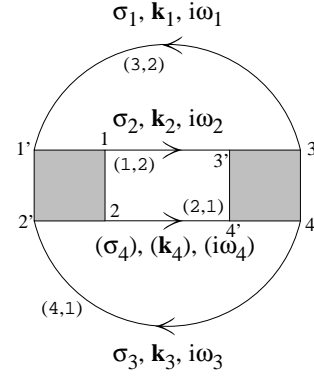


Fig. 15. Diagram of order $|V|^4$ contributing to the thermodynamic potential.

B.2 Two-particle function

We start from the definition of G^{II} in imaginary time (by enclosing σ_4 between parentheses, we mean that its value is to be inferred from that of the other three spins):

$$G_{\sigma_1 \sigma_2, (\sigma_4) \sigma_3}^{\text{II}}(\tau_1, \tau_2; \tau_4, \tau_3) = \langle T_{\tau} c_{\sigma_1}(\tau_1) c_{\sigma_2}(\tau_2) c_{\sigma_3}^{\dagger}(\tau_3) c_{(\sigma_4)}^{\dagger}(\tau_4) \rangle \tag{B.5}$$

and compute it explicitly for any time ordering, using $e^{-(H - \mu N)\tau}$ as evolution operator and inserting complete sets of states as necessary. We then calculate its Fourier transform, defined by the following equation:

$$\int_0^{\beta} d\tau_1 \dots d\tau_4 G_{\sigma_1 \sigma_2, (\sigma_4) \sigma_3}^{\text{II}}(\tau_1, \tau_2; \tau_4, \tau_3) \times e^{i\omega_1 \tau_1 + i\omega_2 \tau_2 - i\omega_3 \tau_3 - i\omega_4 \tau_4} = \tag{B.6}$$

$$\beta \delta(i\omega_1 + i\omega_2 - i\omega_3 - i\omega_4) \times G_{\sigma_1 \sigma_2, (\sigma_4) \sigma_3}^{\text{II}}(i\omega_1, i\omega_2; (i\omega_4), i\omega_3). \tag{B.7}$$

Again, $i\omega_4 = i\omega_1 + i\omega_2 - i\omega_3$. After introducing the following short-hand notation

$$z = 1 + e^{(\mu + h)\beta} + e^{(\mu - h)\beta} + e^{(2\mu - U)\beta}, \tag{B.8}$$

$$x_j^{\pm} = i\omega_j + \mu \pm h, \tag{B.9}$$

$$\bar{x}_j^{\pm} = i\omega_j + \mu \pm h - U, \tag{B.10}$$

the connected correlation functions read:

$$G_{\uparrow\uparrow, \uparrow\uparrow}^{\text{IIC}}(i\omega_1 i\omega_2, (i\omega_4) i\omega_3) = \frac{\beta U^2 n_- (1 - n_-) [\delta(i\omega_2 - i\omega_3) - \delta(i\omega_1 - i\omega_3)]}{x_1^+ \bar{x}_1^+ x_2^+ \bar{x}_2^+}, \tag{B.11}$$

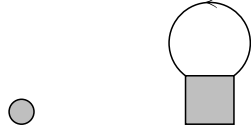


Fig. 16. Diagrams contributing to Γ up to order t_0 .

and

$$G_{\uparrow\uparrow, \downarrow\downarrow}^{\text{IIc}}(i\omega_1 i\omega_2, (i\omega_4) i\omega_3) = \quad (\text{B.12a})$$

$$\frac{n_+ + n_- - 1}{i\omega_1 + i\omega_2 + 2\mu - U} \left(\frac{1}{\bar{x}_1^-} + \frac{1}{\bar{x}_2^+} \right) \left(\frac{1}{\bar{x}_3^+} + \frac{1}{\bar{x}_4^-} \right) \quad (\text{B.12b})$$

$$+ \frac{n_+ - n_-}{i\omega_1 - i\omega_3 - 2h} \left(\frac{1}{\bar{x}_1^-} - \frac{1}{\bar{x}_3^+} \right) \left(\frac{1}{\bar{x}_4^-} - \frac{1}{\bar{x}_2^+} \right) \quad (\text{B.12c})$$

$$+ \frac{\beta U^2 \delta(i\omega_2 - i\omega_3) (e^{(2\mu-U)\beta} - e^{2\mu\beta})}{z^2} \frac{1}{x_1^- \bar{x}_1^- x_2^+ \bar{x}_2^+} \quad (\text{B.12d})$$

$$+ \frac{n_+ - 1}{x_1^- \bar{x}_3^+ x_4^-} + \frac{1 - n_+}{x_1^- \bar{x}_2^+ \bar{x}_3^+} + \frac{1 - n_-}{\bar{x}_1^- x_2^+ \bar{x}_3^+} + \frac{n_- - 1}{x_2^+ \bar{x}_3^+ x_4^-} \quad (\text{B.12e})$$

$$+ \frac{1 - n_-}{\bar{x}_1^- x_2^+ x_4^-} + \frac{1 - n_-}{\bar{x}_1^- x_2^+ \bar{x}_3^+} + \frac{1 - n_-}{\bar{x}_2^+ x_3^+ \bar{x}_4^-} + \frac{n_- - 1}{x_1^- \bar{x}_2^+ x_3^+} \quad (\text{B.12f})$$

All values of $G_{\sigma_1 \sigma_2, (\sigma_4) \sigma_3}^{\text{IIc}}(i\omega_1 i\omega_2, (i\omega_4) i\omega_3)$ can be deduced from equations (B.11–B.12f) above, the antisymmetry with respect to the exchange of two incoming or outgoing variables, and the possibility to exchange \uparrow and \downarrow by doing $h \rightarrow -h$.

Apart from the regular terms of lines (B.12e, B.12f), G^{IIc} contains only singular or possibly singular terms. Indeed, line (B.12d) has $\delta(i\omega_2 - i\omega_3)$ in factor, line (B.12b) becomes proportional to $\delta(i\omega_1 + i\omega_2)$ in the half-filling limit, and line (B.12c) becomes proportional to $\delta(i\omega_1 - i\omega_3)$ in the zero magnetic field limit. These special cases have to be properly taken into account while computing G^{IIc} directly at half-filling and zero magnetic field.

Appendix C: A practical test of the method

In this section, we test the diagrammatic theory and the continued fraction representation on an exactly solvable simple model. We consider the atomic limit itself, with a slight doping given by a chemical potential $\mu = u + t_0$. On the one hand, we know the exact Green function from

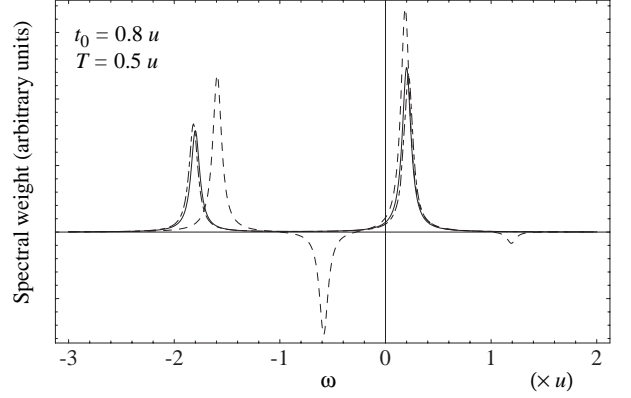


Fig. 17. Spectral function of the atomic model with chemical potential $\mu = 1.8u$ at temperature $T = 0.5u$. Comparison between the exact result (solid), the raw approximation (dashed), and the continued fraction (dot-dashed). Whereas the dashed curve is neither normalized, nor even positive, the difference between the other two curves is hardly noticeable.

equation (B.4):

$$G_{\text{ex}}(i\omega) = \frac{1 - n}{i\omega + u + t_0} + \frac{n}{i\omega - u + t_0}, \quad (\text{C.1})$$

with

$$n = \frac{e^{(u+t_0)\beta} + e^{2t_0\beta}}{1 + 2e^{(u+t_0)\beta} + e^{2t_0\beta}}. \quad (\text{C.2})$$

On the other hand, if we consider the chemical potential shift as a zero-range hopping perturbation, we can compute Γ to first order in powers of t_0 with the help of the diagrams depicted in Figure 16, and obtain

$$\Gamma^{(1)}(i\omega) = \frac{i\omega}{(i\omega)^2 - u^2} + \frac{-t_0 u^2}{((i\omega)^2 - u^2)^2} + \frac{t_0 \beta u n_{\text{F}}(u)}{(i\omega)^2 - u^2}, \quad (\text{C.3})$$

where n_{F} is the Fermi occupation factor. It is straightforward to check that the exact Green function and the “raw” approximation given by the above value of Γ

$$G_{\text{raw}}^{(1)}(i\omega) = \frac{1}{\Gamma^{(1)}(i\omega)^{-1} + t_0}, \quad (\text{C.4})$$

coincide up to order t_0 included. But this expansion of Γ , although undoubtedly correct, leads to the general causality problem described in Section 3.1.

On the other hand, the reconstructed continued fraction is

$$G_J^{(1)}(i\omega) = \frac{1}{i\omega + (1 - \beta u n_{\text{F}}(u))t_0 - \frac{u^2}{i\omega + (1 + \beta u n_{\text{F}}(u))t_0}}. \quad (\text{C.5})$$

Figure 17 shows a comparison between the spectral weight of the exact solution, the raw approximation, and the final

continued fraction. One can see that $G_J^{(1)}(i\omega)$ yields an extremely good spectral function (which remains true at any temperature and for a very wide range of values of t_0).

Nonetheless, our enthusiasm has to be tempered by the following remarks. First, the exact solution being a two-pole rational function, it is not surprising that a finite continued fraction is able to mimic it satisfactorily. Secondly, going to low temperature does no harm in this case, but the two-site problem, described in Appendix D.2, shows that this is not true in general.

Appendix D: Higher loops and the two-site problem

D.1 Order t^4 and order t^5

Figure 18 shows the diagrams contributing to fourth and fifth order. The diagrams of Figure 18 lead to the following expression for Γ :

$$\begin{aligned} \Gamma^{(4)}(\mathbf{k}, i\omega) = & \frac{i\omega}{(i\omega)^2 - 1} + \frac{6dt^2 i\omega}{((i\omega)^2 - 1)^3} \\ & + 6c(\mathbf{k})t^3 \left(\frac{\beta(-1 + e^\beta)}{2(1 + e^\beta)} \frac{2(i\omega)^2 - 1}{((i\omega)^2 - 1)^2} \frac{2(i\omega)^2 - 1}{((i\omega)^2 - 1)^4} \right) \\ & + t^4 \left\{ \frac{3\beta^2 d(-1 + 2d)e^\beta(i\omega)}{(1 + e^\beta)^2 (i\omega - 1)^3 (i\omega + 1)^3} \right. \\ & + \frac{3\beta d(-1 + e^\beta)i\omega}{(1 + e^\beta)^3 (i\omega - 1)^4 (i\omega + 1)^4} \\ & \times (-2 - 13e^\beta + 18de^\beta - 2e^{2\beta} + 2(i\omega)^2 \\ & + e^\beta(i\omega)^2 + 6de^\beta(i\omega)^2 + 2e^{2\beta}(i\omega)^2) \\ & + \frac{3di\omega}{2(1 + e^\beta)^2 (i\omega - 3)(i\omega - 1)^5 (i\omega + 1)^5 (i\omega + 3)} \\ & \times \left[(247 - 278d + 914e^\beta - 1396de^\beta + 247e^{2\beta} - 278de^{2\beta}) \right. \\ & + (15 - 378d + 450e^\beta - 1596de^\beta + 15e^{2\beta} - 378de^{2\beta})(i\omega)^2 \\ & + (-3 + 42d - 90e^\beta + 252de^\beta - 3e^{2\beta} + 42de^{2\beta})(i\omega)^4 \\ & \left. \left. + (-3 + 6d + 6e^\beta - 12de^\beta - 3e^{2\beta} + 6de^{2\beta})(i\omega)^6 \right] \right\}, \end{aligned} \quad (\text{D.1})$$

where we have set $u = 1$. The fifth order and the corresponding continued fraction are too lengthy to be presented here, but are available on the internet [51].

D.2 The two-site problem

The exactly solvable two-site problem provides a good testing ground for the higher-order results just obtained. In this subsection the parameter t is replaced by $t/2$ in order to account for periodic boundary conditions on a lattice with only two sites (say site 1 and site 2). The analytic

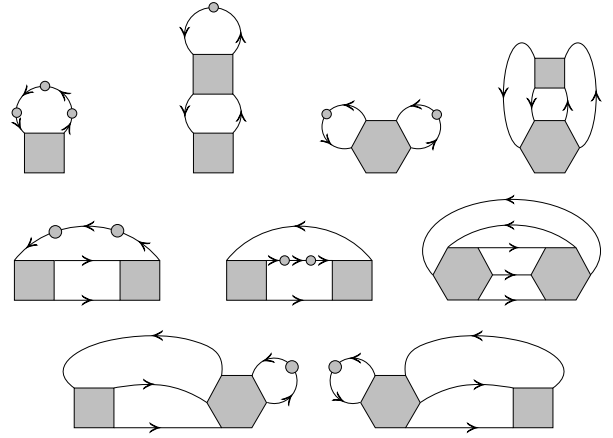


Fig. 18. Diagram contributing to Γ at fourth order (top row) and fifth order (bottom two rows).

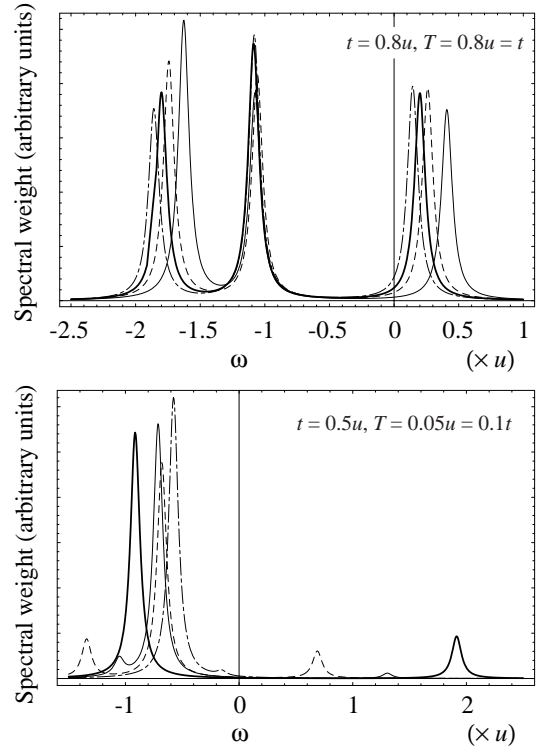


Fig. 19. Above: Spectral function $A(k = 0, \omega)$ of the two-site Hubbard model with hopping term $t = 0.8u$ at temperature $T = t = 0.8u$. Comparison between the exact result (bold) and the continued fraction at third (solid), fourth (dashed) and fifth (dot-dashed) order. In this region of parameter space, the approximation improves with increasing order. Below: The same, but with $t = 0.5u$ at temperature $T = 0.1t = 0.05u$. In this region of parameter space, the third-order approximation is the best one.

expressions $\mathcal{G}_{11}(i\omega)$ and $\mathcal{G}_{12}(i\omega)$ of the Green function are available. Replacing the momentum integrations by sums over the two values $k = 0$ and $k = \pi$, the expansion of \mathcal{G}_{11} up to order t^5 has been computed in the usual way (similar to what was done in the previous subsection), and checked to be the same as the one obtained from the exact solution. Furthermore, it leads to a continued fraction having only

four floors instead of eight, as it should since the exact solution has four poles. It is then possible to investigate the validity of the various approximations throughout the (T, t) plane. Empirically, we were led to following conclusion: for $T > t$ the approximation manifestly improves with the order, and for $T \leq t$ the approximation deteriorates much faster with increasing order. Two examples illustrating this behavior are shown in Figure 19.

References

1. L.D. Landau, Sov. Phys. JETP **3**, 920 (1957).
2. L.D. Landau, Sov. Phys. JETP **5**, 101 (1957).
3. J. Hubbard, Proc. R. Soc. (London) Ser. A **276**, 238 (1963).
4. E.H. Lieb, F.Y. Wu, Phys. Rev. Lett. **20**, 1445 (1968).
5. S. Tomonaga, Prog. Theor. Phys. **5**, 544 (1950).
6. J.M. Luttinger, J. Math. Phys. **4**, 1154 (1963).
7. J. Sólyom, Adv. Phys. **28**, 201 (1979).
8. C. Bourbonnais, L.G. Caron, Int. J. Mod. Phys. B **5**, 1033 (1991).
9. R. Shankar, Rev. Mod. Phys. **66**, 129 (1994).
10. H. Frahm, V.E. Korepin, Phys. Rev. B **42**, 10553 (1990).
11. H. Frahm, V.E. Korepin, Phys. Rev. B **43**, 5653 (1991).
12. H.J. Schulz, in *Les Houches, Session LXI (1994)*, edited by E. Akkermans *et al.* (Elsevier, Amsterdam, 1995), p. 533.
13. A.V. Chubukov, D. Pines, B.P. Stojković, J. Phys. Cond. Matt. **8**, 10017 (1996), and references Iye 1992 and Ong 1990 included therein.
14. F. Gebhard, *The Mott Metal-Insulator Transition* (Springer, Berlin, 1997).
15. J. Favand *et al.*, Phys. Rev. B **55**, R4859 (1997).
16. S.E. Barnes, J. Phys. F **6**, 1375 (1976).
17. P. Coleman, Phys. Rev. B **28**, 5255 (1983).
18. G. Kotliar, A.E. Ruckenstein, Phys. Rev. Lett. **57**, 1362 (1986).
19. Y.M. Vil'k, A.-M.S. Tremblay, J. Phys. I France **7**, 1309 (1997).
20. N. Bulut, D.J. Scalapino, S.R. White, Phys. Rev. B **50**, 7215 (1994).
21. E. Dagotto, A. Nazarenko, M. Boninsegni, Phys. Rev. Lett. **73**, 728 (1994).
22. K. Kobayashi *et al.*, Phys. Rev. Lett. **82**, 803 (1999).
23. A. Moreo *et al.*, Phys. Rev. B **41**, 2313 (1990).
24. R. Preuss *et al.*, Phys. Rev. Lett. **73**, 732 (1994).
25. R. Preuss, W. Hanke, W. von der Linden, Phys. Rev. Lett. **75**, 1344 (1995).
26. W. Metzner, D. Vollhardt, Phys. Rev. Lett. **62**, 324 (1989).
27. T. Pruschke, D.L. Cox, M. Jarrell, Phys. Rev. B **47**, 3553 (1993).
28. A. Georges *et al.*, Rev. Mod. Phys. **68**, 13 (1996).
29. D.E. Logan, P. Nozières, Philos. Trans. R. Soc. Lond. A **356**, 249 (1998).
30. R.M. Noack, F. Gebhard, Phys. Rev. Lett. **82**, 1915 (1999).
31. A.B. Harris, R.V. Lange, Phys. Rev. **157**, 295 (1967).
32. K. Kubo, Prog. Theor. Phys. **64**, 758 (1980).
33. K.K. Pan, Y.L. Wang, Phys. Rev. B **43**, 3706 (1991).
34. M. Bartkowiak, K.A. Chao, Phys. Rev. B **46**, 9228 (1992).
35. C. Bourbonnais, Ph.D. thesis, Université de Sherbrooke, 1985.
36. S.K. Sarker, J. Phys. C **21**, L667 (1988).
37. S. Pairault, D. Sénéchal, A.-M.S. Tremblay, Phys. Rev. Lett. **80**, 5389 (1998).
38. J. Voit, Rep. Prog. Phys. **57**, 977 (1994).
39. J. Voit, in *Proceedings of The Ninth International Conference on Recent Progress in Many-Body Theories, Sydney*, edited by D. Neilson (World Scientific, Singapore, 1998).
40. C. Kim *et al.*, Phys. Rev. Lett. **77**, 4054 (1996).
41. K. Kobayashi *et al.*, Phys. Rev. Lett. **82**, 803 (1999).
42. B.O. Wells *et al.*, Phys. Rev. Lett. **74**, 964 (1995).
43. P.W. Leung, B.O. Wells, R.J. Gooding, Phys. Rev. B **56**, 6320 (1997).
44. Ph. Brune, A.P. Kampf, cond-mat/0001210 (unpublished).
45. W. Metzner, Phys. Rev. B **43**, 8549 (1991).
46. D. Boies, C. Bourbonnais, A.-M.S. Tremblay, Phys. Rev. Lett. **74**, 968 (1995).
47. The $1/(R!)^2$ prefactor corrects equation (5) of reference [46], where $1/(n!)^2$ should have appeared.
48. J. Giliewicz, *Approximants de Padé* (Springer-Verlag, Berlin, 1978), Vol. 667.
49. A. Georges, W. Krauth, Phys. Rev. B **48**, 7167 (1993).
50. J.W. Negele, H. Orland, *Quantum many-particle systems* (Addison-Wesley, New York, 1988).
51. S. Pairault, Mathematica™ notebook at <http://www.physique.usherb.ca/~dsenech/pairault.nb>
52. D. Poulin, S. Pairault, D. Sénéchal, A.-M.S. Tremblay (unpublished).
53. M. Jarrell, J. Gubernatis, Phys. Rep. **269**, 133 (1996).
54. A. Georges, W. Krauth, Phys. Rev. Lett. **69**, 1240 (1992).
55. S. Allen (private communication, unpublished).
56. A.-M. Daré, G. Albinet, Phys. Rev. B **61**, 4567 (2000).
57. M. Meinders, H. Eskes, G. Sawatzky, Phys. Rev. B **48**, 3916 (1993).
58. According to Rozenberg *et al.* (Phys. Rev. Lett. **83**, 3498 (1999)), if antiferromagnetism is frustrated, there is a first-order Mott transition, but it occurs in a regime ($T < t$) inaccessible to our approach. For $T > t$, we are above the critical point, where the change from metal to insulator is a crossover. Note that Schlipf *et al.* (Phys. Rev. Lett. **82**, 4890 (1999)) argue rather that the transition is not of first order.
59. V.S. Viswanath, G. Müller, *The Recursion Method, Lecture Notes in Physics* (Springer-Verlag, Berlin, New York, 1994).
60. D. Sénéchal, D. Perez, M. Pioro-Ladrière, Phys. Rev. Lett. **84**, 522 (2000).
61. A.A. Abrikosov, L.P. Gorkov, I.E. Dzyaloshinski, *Methods of Quantum Field Theory in Statistical Physics* (Dover, New York, 1963).